The Thesis committee for Jason Christopher Soric Certifies that this is the approved version of the following thesis:

Epsilon-Near-Zero Waveguide-to-Coaxial Matching and Multiband Gap Launcher Antenna

APPROVED BY

SUPERVISING COMMITTEE:

John H. Davis, Co-supervisor

Andrea Alú, Co-supervisor

Epsilon-Near-Zero Waveguide-to-Coaxial Matching and Multiband Gap Launcher Antenna

by

Jason Christopher Soric, B.S.E.E.

THESIS

Presented to the Faculty of the Graduate School of

The University of Texas at Austin

in Partial Fulfillment

of the Requirements

for the Degree of

MASTER OF SCIENCE IN ENGINEERING

THE UNIVERSITY OF TEXAS AT AUSTIN

December 2010

This work is dedicated to my mother, Dana G. Hill, and my grandfather, Jack T. Hill.

Acknowledgments

This work would not be possible without the gracious support of my professors Dr. John Davis and Dr. Andrea Alú. Dr. John Davis' experimental knowledge and Dr. Alú's theoretical support were both invaluable in this work, and for that I am totally grateful.

To my closest friends and collegues: thank you for reminding me to enjoy life, especially in difficult times. Additionally, thank you to all of the professors and managers that have given me so many opportunities and helped me to reach my academic and professional goals.

Epsilon-Near-Zero Waveguide-to-Coaxial Matching and Multiband Gap Launcher Antenna

Jason Christopher Soric, M.S.E.
The University of Texas at Austin, 2010

Supervisors: John H. Davis
Andrea Alú

The design and use of metamaterials have shown exciting applications in electrical engineering, physics, optics, and other science fields that are expanding our physical understanding and leading to unprecedented performance of many standard devices such as antennas, microwave circuits, and sensors. The manufacturing of metamaterials, while ingenious, has typically been exotic and depended on the inclusion of sub-wavelength particles in a host medium to tailor the effective characteristics of a material. This work verifies a much more simple approach to realizing a kind of metamaterial, the epsilon-near-zero (ENZ) metamaterial. The intriguing aspect of this metamaterial is that while it is simple to realize, it is a novel approach to many practical applications such as the tunneling energy through highly discontinuous bends and abruptions, cloaking of sensors, miniaturization of microwave components, and design of highly directive antennas. Further, the physics and mathematical formulation of these ENZ materials is both intriguing and counterintuitive.

Table of Contents

List of Tables

List of Figures

Chapter 1

The Epsilon-Near-Zero Tunneling Phenomenon

1.1 Background

Electromagnetic metamaterials are effectively homogenized electromagnetic structures with unusual properties not readily available in nature. An effectively homogeneous structure is a structure whose structural average cell size is much smaller than the guided wavelength (usually taken as much less than a quarter guided wavelength.) This implies electronic metamaterials are: "*distributed structures constituted of lumped elements, and the electromagnetic waves are essentially myopic to the lattice*" [1, 2]. But more broadly is defined by materials which are engineered to tailor properties that serve a scientific purpose, thus this includes electrical engineering, optics, physics, chemistry, and nanotechnology.

The pioneers of metamaterials sought to create materials to solve difficult and practical problems with extraordinary results. Successful studies and experiments such as microwave simulations of plasmas, and imaging that exceeds the diffraction limit using evanescent modes are given by the groundbreaking work in [3, 4], respectively. The first experimental verification of a

simultaneously negative permittivity and permeability material, Veselago material, was demonstrated by D.R. Smith [5]. Rather recently these concepts have been expanded and used in applications such as microstrip patch antenna miniaturization, increased directivity, microwave component optimization, radar and acoustic cloaking, near-field imaging, and sensor phase pattern tailoring, to name a few [1]-[8].

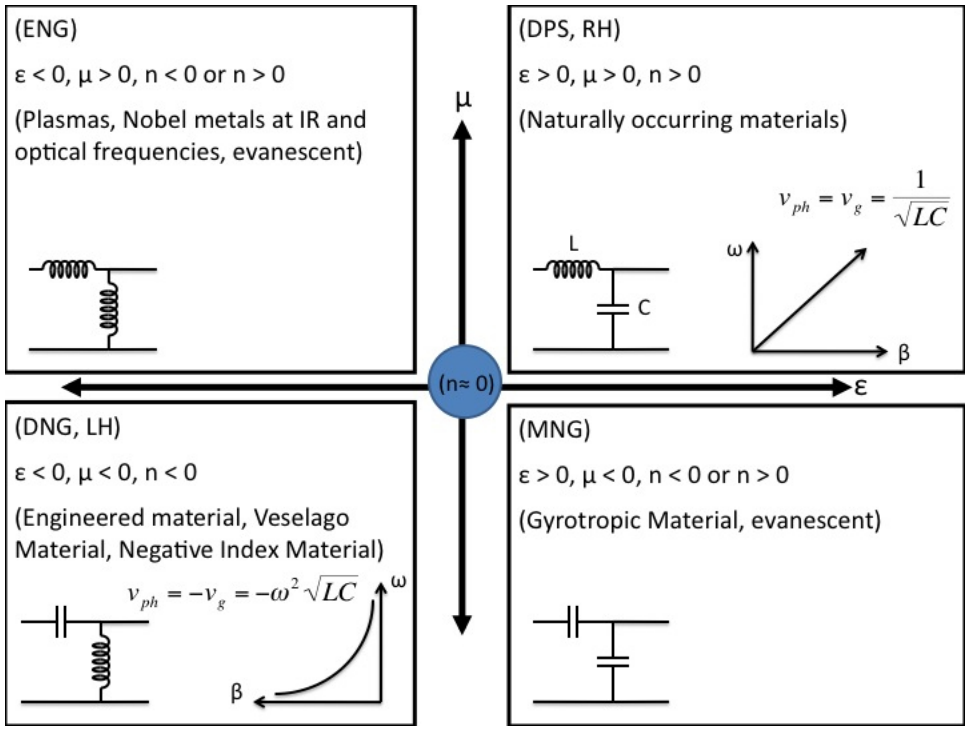

Figure 1.1: Categorization of electromagnetic materials

In figure 1.1 and table 1.1, we can see that double positive (DPS), or right-handed (RH) materials are the usual materials where ϵ and μ are both positive, which leads to the standard right-handed triad in electromagnetic analysis and implies propagating waves. This media can also be modeled by

Table 1.1: Wave propagation properties of effective materials

	DPS	ENG	DNG	MNG
Re[η]	+	+	+	+
Im[η]	$\pm$	+	$\mp$	-
Re[$\mathbf{k}$]	+	$\pm$	-	$\mp$
Im[$\mathbf{k}$]	-	-	-	-

transmission-line analysis, where L and C are per unit length material and geometrical parameters [9] and [10]. In these materials, unbounded waves propagate with a phase velocity v_{ph} that is equal to the group velocity v_g.

DNG materials, also called left-handed (LH), or backward-wave materials were shown by Veselago in 1968, and are characterized by "*substances with simultaneously negative values of* ϵ *and* μ" [11]. These materials have gained the most attention in the engineering and physics communities, since unlike the ENG and MNG materials, the DNG supports wave propagation but in a very unusual way. These materials form a left-handed triad, and therefore lead to backward-wave propagation, which is shown by anti-parallel phase and group velocities. This counterintuitive behavior predicted by Veselago has led to applications such as reverse Doppler and sub-diffraction resolution lenses.

ENG materials can be found in nature in noble metals at high frequencies and also occurs in the ionosphere for radio waves, since the ionosphere is a plasma, or a *sea of free electrons*. This behavior is predicted by the Drude dispersive model for the effective permittivity of the ionosphere. Since the index of refraction for an ENG material is negative and imaginary, this leads

to evanescent waves. ENG materials can also be modeled by transmission line analysis, were a negative shunt C becomes an effective shunt L. A transverse electric (TE) polarization in a waveguide also can be modeled as an ENG material, where the transverse wave vector component k_t is greater than wavenumber k.

The MNG material is the dual of the ENG material and can be modeled as a transmission line as well. Additionally, a transverse magnetic (TM) wave can be modeled in a waveguide under the same condition as the ENG model; i.e., $k_t > k$. Like ENG materials, waves do not propagate and are evanescent.

While much research and attention has been focused on DNG, ENG, and MNG metamaterials, this work describes a subset of metamaterials titled epsilon-near-zero metamaterials. Figure 1.1 and table 1.1 provides little information about ENZ structures under study in this work. This is because the attribute of the ENZ of most interest is the tunneling of electromagnetic energy with a *static* phase velocity independent of the geometry of the tunneling cavity. The exact basis of this work is the idea of *supertunneling* electromagnetic energy through arbitrary transitions and bends. This *supertunneling* occurs at frequencies where the effective permittivity of a material is near zero and can be seen as the middle point of figure 1.1. Since the index of refraction is zero, or near zero, this implies that either the permittivity or the permeability can be zero; however, this work will focus on structures with ϵ-near-zero.

1.2 Anomalous Supertunneling and the ENZ Waveguide Interface Problem

Excellent work is provided in [12, 13, 14] which gives rigorous, closed-form, analytic equations fully characterizing the tunneling of electromagnetic energy through general, lossless ENZ transitions. Loss can be considered, but its analysis only slightly affects the equations and was shown to be negligible in ENZ scenerios [14], so the same physical behavior can be studied without loss of generality. These works provided the equation for the reflection coefficient for the entrance of a waveguide to an arbitrary $\epsilon = 0$ channel, which is given in equation 1.1.

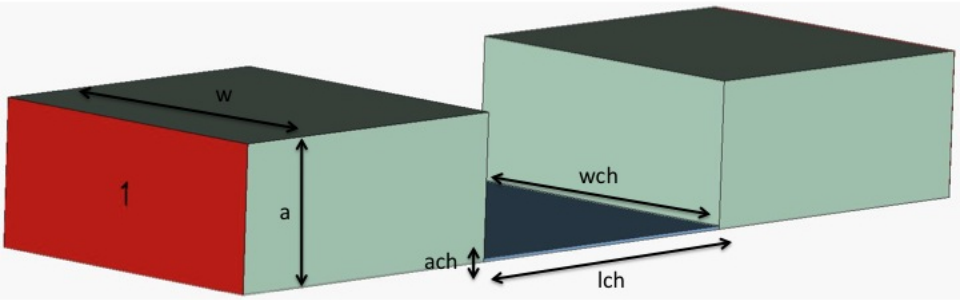

Figure 1.2: Rectangular waveguides connected by ENZ channel

$$\Gamma = \frac{(a_1 - a_2) - jk_0\mu_r A_p}{(a_1 + a_2) + jk_0\mu_r A_p} \tag{1.1}$$

Here, k_0 is the free space wave number, μ_r is the relative permeability of the $\epsilon = 0$ channel, a_1 and a_2 are the heights of the outer wave guiding sections, and A_p is the cross-sectional area of the $\epsilon = 0$ channel, defined as

$a_{ch}l_{ch}$. For clarity, the reflection coefficient in equation 1.1 is taken as looking into the $\epsilon = 0$ channel from the outer waveguide in figure 1.2.

It can be shown, by setting equation 1.1 equal to zero, for $a_1 = a_2 =$ a, two solutions exist to make the reflection coefficient go to zero, and make possible total transmission through the $\epsilon = 0$ channel, namely, $\mu_r = 0$ or $\frac{a_{ch}l_{ch}}{a} \ll 1$. The latter is the case studied in this work. The second case shows that the transmission coefficient, $\tau = 1 + \Gamma$, approaches one as the $\epsilon = 0$ cross-sectional area becomes vanishingly small. This is both a remarkable and counterintuitive result.

1.2.1 Realization of an ENZ metamaterial

A rectangular waveguide operated at cutoff will yield an ENZ metamaterial structure. This is primarily because an effective propagation constant and characteristic impedance can be derived as a medium that supports transverse-electromagnetic (TEM) wave propagation. As discussed in the background section, the medium has been *homogenized*. As will be shown, the wavelength of this ENZ rectangular waveguide is infinite; therefore, the ENZ channel will be will be myopic to the impinging wave. Additionally, the condition of the effective permittivity being near zero at radio and microwave frequencies only occurs in nature in very unique cases such as the ionosphere. What's more, by using the dispersive characteristics of a rectangular waveguide operated at, or near cutoff, there is no need for complex sub-wavelength inclusions.

1.2.1.1 Effective permittivity of a rectangular waveguide

This work is based on the pioneering work of Rotman [3]. In his work, Rotman analytically formulated equations for microwave structures using 2D and 3D rodded grid arrays and parallel-plate waveguides to simulate plasmas. Alú and Silveirinha, and Engheta further developed this theory and applied it to ENZ metamaterials [12].

Starting with the wave number for a rectangular waveguide, we can derive the effective parameters for the ENZ channel.

$$\beta_{eff}^2 = \omega^2 \mu \epsilon_{eff} = k_{ch}^2 - k_c^2 \tag{1.2}$$

Then for the mono-modal TE_{10} propagation under consideration,

$$\epsilon_{eff} = \epsilon_{ch} \left[1 - \left(\frac{\lambda_{ch}}{2w_{ch}} \right)^2 \right] \tag{1.3}$$

From equation 1.3, we can see that the effective permittivity of the rectangular waveguide can be made to be zero when we are under mono-modal TE_{10} propagation; and the width of the ENZ channel is $\frac{\lambda_{ch}}{2}$, which implies the waveguide is cutoff. It is also interesting to point out that w_{ch} from figure 1.2 is a degree of freedom for the *tuning* of the ENZ condition, and the ENZ frequency corresponds to the plasma frequency in the Drude model.

1.2.1.2 Transverse characteristic impedance

Transmission line analysis is a very important tool for the microwave engineer, since it lends itself to mathematical and circuit abstraction, while en-

capsulating the salient features of field-analysis. The characteristic impedance of a medium is defined in terms of forward or reflected voltage and current waves. In the lossless limit, under consideration in this work, $Z_0 = \frac{V^+}{I^+} = -\frac{V^-}{I^-}$. For non-TEM type propagation such as TE_{mn} or TM_{mn}, unique voltages and currents are not defined. However, if we consider only the transverse components; i.e., E_t and H_t, then an effective characteristic impedance can be defined for conventional transmission line analysis. Only the transverse components contribute to the actual power flow in the waveguide, so the transverse components are the most relevant for wave-guiding structures. Moreover, we can define the TE_{10} characteristic impedance using static relations.

$$Z_{ENZ} = \frac{a_{ch}}{w_{ch}} \frac{\mu_0 \omega}{\beta_{10}^{ch}} \tag{1.4}$$

$$Z_{out} = \frac{a}{w} \frac{\mu_0 \omega}{\beta_{10}^{wg}} \tag{1.5}$$

The algebra for equation 1.5 is exactly the same as from equation 1.4. In equation 1.4, it is clear that Z_{ENZ} will be infinite at the cutoff frequency, but not at other frequencies. These equations will aid us in developing a transmission line model for the system in Fig. 1.2. These equations are also necessary for matching a coaxial cable using an ENZ channel to outer waveguide sections or an antenna, which will be studied later in this work.

1.2.2 Transmission line model for E and H-Plane discontinuities of a rectangular waveguide with an ENZ channel

Work by Alú [12] developed a transmission-line model for the ENZ channel. In [12], a transmission-line model was drawn that accounted for the E-plane discontinuities of the entrance and exit of the ENZ channel. Alú's worked provided great insight into possible resonances in the ENZ channel. A similar approach is taken in this work, which also takes into account the H-plane step that is needed for our air-filled ENZ experimental structure. The equivalent transmission line model for the waveguide section to be studied for the experiment in Chapter 2 is given in figure 1.3. Here, β_{out}, Z_{out}, and l_{out} refer to the outer waveguide sections; β_{eff}, Z_{ENZ}, and l_{ch} refer to the ENZ channel. Z_{diss} is the equivalent lumped-element reactive components used to represent the excited higher order modes due to the discontinuities at the waveguide/ENZ entrances. For E and H-plane discontinuities, which will be studied in-depth in the experimental section of this work, $Z_{diss} = \frac{-j}{\omega C} + j\omega L$.

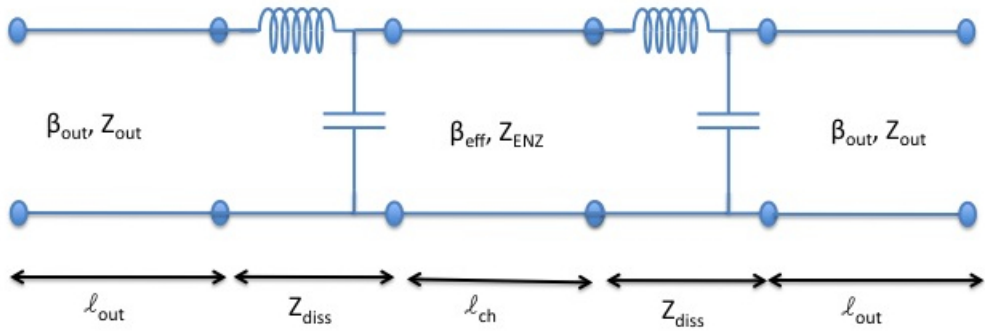

Figure 1.3: Equivalent transmission line model of rectangular waveguides with an ENZ channel

$$Z_{diss} = \frac{-j}{\omega C} + j\omega L \tag{1.6}$$

$$Z_{l,right} = \frac{Z_{diss} Z_{out}}{Z_{diss} + Z_{out}} \tag{1.7}$$

$$Z_{in} = Z_{ENZ} \frac{Z_{l,right} + jZ_{ENZ} \tan(\beta_{eff} l_{ch})}{Z_{ENZ} + jZ_{l,right} \tan(\beta_{eff} l_{ch})} \tag{1.8}$$

$$Z_{l,left} = \frac{Z_{in} Z_{diss}}{Z_{in} + Z_{diss}} \tag{1.9}$$

$$\Gamma = \frac{Z_{l,left} - Z_{out}}{Z_{l,left} + Z_{out}} \tag{1.10}$$

$$\Gamma = -\frac{\tan(\beta_{eff} l_{ch}) \left[Z_{ENZ}^2 \left(C^2 Z_{out}^2 + B^2\right) - Z_{out}^2 B^2\right] + 2CZ_{ENZ} Z_{out}^2 B}{2Z_{ENZ} Z_{out} B \left[CZ_{out} + jB\right] - \tan(\beta_{eff} l_{ch}) \left[Z_{out}^2 B^2 + Z_{ENZ}^2 \left[jCZ_{out} - B\right]^2\right]} \tag{1.11}$$

In equation 1.11, B = $\omega LC - 1$. To solve for the supertunning transmission, we will set $\Gamma = 0$, and investigate the conditions for this anomalous tunneling. We can assume that L and C ≈ 0, since we know the effects of these reactances is to slightly detune the resonance; i.e., C will tune the frequency down, and L will tune the frequency up. A mode-matching technique could be used to determine any reactance value based on the type of waveguide geometry used. With this assumption, the physics is much more clear.

$$\Gamma = \tan(\beta_{eff} l_{ch}) \left[Z_{ENZ}^2 \left(C^2 Z_{out}^2 + B^2 \right) - Z_{out}^2 B^2 \right] + 2C Z_{ENZ} Z_{out}^2 B = 0 \quad (1.12)$$

There are two solutions to equation 1.12, and both will be important in the following sections of this work.

1. $\tan(\beta_{eff} l_{ch}) = 0 \implies l_{ch} = \frac{\lambda_{ch} n}{2}$, where n $\in$ 0,1,2,... These are the Fabry-Perot resonances, where $\lambda_{ch} = \frac{\lambda_0}{\sqrt{1-\left(\frac{f_c}{f}\right)^2}}$, and $\lambda_0 = \frac{c}{f_0}$ is the unbounded wavelength at a given operating frequency. It is also noted that β_{eff} is not equal to zero, since ϵ_{eff} is not necessarily equal zero at these Fabry-Perot resonances.

2. $Z_{out} = Z_{ENZ} \implies$ ENZ tunneling

1.2.3 Electric field enhancement

One of the central characteristics of the ENZ channel is that of having an enormous electric field enhancement inside the ENZ cavity. This enhancement can be proved by the continuity of the voltage between the outer waveguide and the ENZ waveguide connected to it [12]. This is given by considering only the transverse electric field components of the TE_{10} at the boundary. In this case, we can use the static relationship E_t^{inc}a = $E_t^{ch} a_{ch}$, which leads to equation 1.13.

$$E_y \approx \frac{a}{a_{ch}} E_y^{inc}|_{x=0} \quad (1.13)$$

Using the full-wave simulator CST, we can verify these derivations with two waveguides connected by a rectangular waveguide operated at its cutoff. The waveguide dimensions were taken from [15] for this initial study. Referring back to figure 1.2, the outer waveguides are filled with Teflon ($\epsilon_r = 2.1$) to have a lower cutoff frequency than the ENZ channel. The dimensions of the outer waveguides are: a = 44.5 mm, $w = w_{ch} = 100$ mm, $l_{wg} = l_{ch} = 100$ mm. The height of the ENZ channel is $a_{ch} = 1$ mm. The ENZ waveguide is filled with air. With these dimensions, $f_c^{ENZ} = 1.5$ GHz, $f_c^{OUTER} = 1.04$ GHz.

Since there is only an E-plane step, the operating frequency will be slightly de-tuned due to a capacitive localized reactance at the discontinuity. At the tunneling frequency of 1.45 GHz, we can see that there is an extreme enhancement of the electric field across the ENZ cavity shown in figure 1.4.

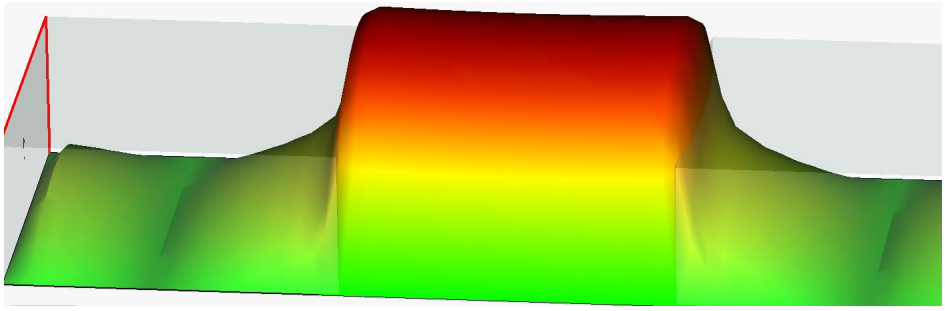

Figure 1.4: Electric field enhancement in ENZ cavity

1.2.4 Infinite phase velocity in the ENZ cavity and comparisons to Fabry-Perot resonances

One of the most interesting aspects of the an ENZ resonance, and one that strongly differentiates it from a Fabry-Perot resonance is that the wave

inside the ENZ channel has static-like properties [12]. Figure 1.5 shows the scattering parameters of the waveguide simulation in figure 1.2. There are two distinct resonances. The first is due to ENZ channel, as predicted from the calculations from the dimensions of the waveguides, and the second is due to the Fabry-Perot phenomenon. In a Fabry-Perot resonator, the resonance is highly dependent on the length of the channel since it is due to the interference of incident and reflected waves inside the cavity, and this occurs and integer multiples of half the wavelength. These resonances were discussed in section 1.2.2, and were the result of equation 1.12. Therefore, the wave in the cavity is a standing wave, with strong amplitude variation. This can be seen in figure 1.6, where the electric field has been taken across the waveguide channel using full-wave electromagnetic simulations. Here, we can clearly see the half-wave interference, and the electric field does not have a static nature.

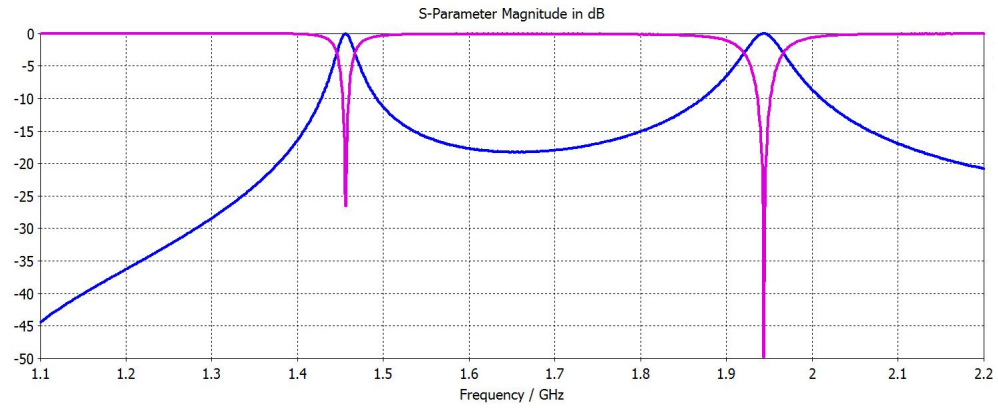

Figure 1.5: Scattering parameters of waveguide-to-waveguide transition

The ENZ approach has an acutely different physics associated with it. In particular, since the effective permittivity of the metamaterial is close to

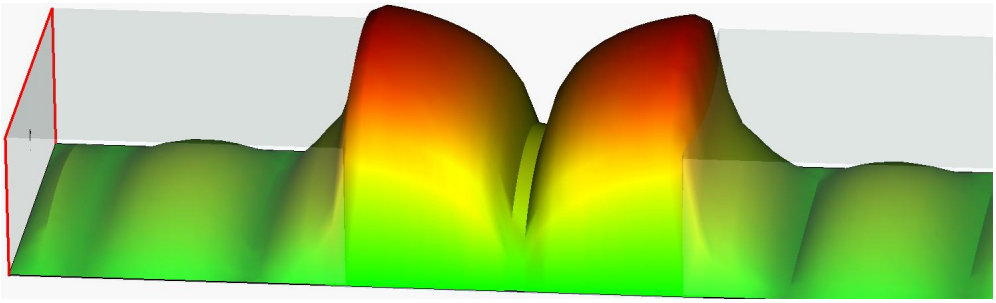

Figure 1.6: Electric field of Fabry-Perot resonance

zero, the phase velocity is infinite, which leads to a static-like electric field behavior across the ENZ cavity in planes that are longitudinal to the wave propagation. However, the transverse wave characteristic is still maintained across the cavity. This constant enhanced electric field in the ENZ cavity could be used for a number of applications including microwave heating and matching. From figure 1.4, this lack of phase variation across the channel lends itself as another degree of freedom for the engineer.

Chapter 2

Experimental Verification of the Supercoupling Effect Through an ENZ Channel

2.1 Waveguide Matching Using an ENZ Cavity

The goal of this chapter is to apply concepts introduced in Chapter 1 to an experimental setup. While the theory was developed in the first chapter, we would like use the design rules established in the literature, and take experimental data. In this experimental example, we will demonstrate energy coupling between two rectangular waveguides connected by an ENZ cavity. Simulation and experimentation is the focus of this chapter.

2.1.1 Waveguide supercoupling using ENZ matching

In this section, we will experimentally show the anomalous wave transmission between two rectangular waveguides connected via an ENZ channel operated at cutoff. All of the waveguides are air-filled, so the ENZ section will have $w_{ch} < w$ in order to have a higher cutoff than the outer waveguides rather than using a dielectric material. Since the waveguides have both an E-plane and a H-plane discontinuity, the operating frequency will be closer to the designed cutoff frequency. This is due to an effective conjugate match

at the junction between the excited reactances and can be seen in equation 1.6. Similar experiments were also verified independently by the University of Pennsylvania and Duke University [16, 17, 18]. In [16, 17], rectangular waveguides were used with various ENZ geometries, which verified the anomalous energy tunneling. In [18], a monolithic complementary split ring resonator was employed as the ENZ channel.

2.1.2 Experimental setup

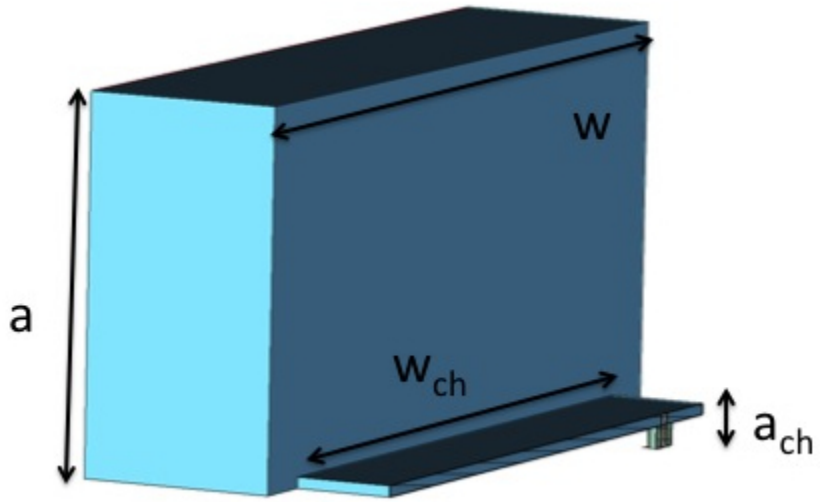

Figure 2.1: Coaxial matching to outer rectangular waveguides

Referring to Fig. 2.1, $w = 72$ mm, $w_{ch} = 61$ mm, a = 34 mm, and $a_{ch} = 1$ mm. In figures 2.2 through 2.3, each rectangular waveguide slot is equal, and are used for changing the length and phase of the channel and outer waveguide sections. Each of these slots = 18 mm. With these dimensions, $f_c^{out} = 2.08$ GHz and $f_c^{ENZ} = 2.46$ GHz.

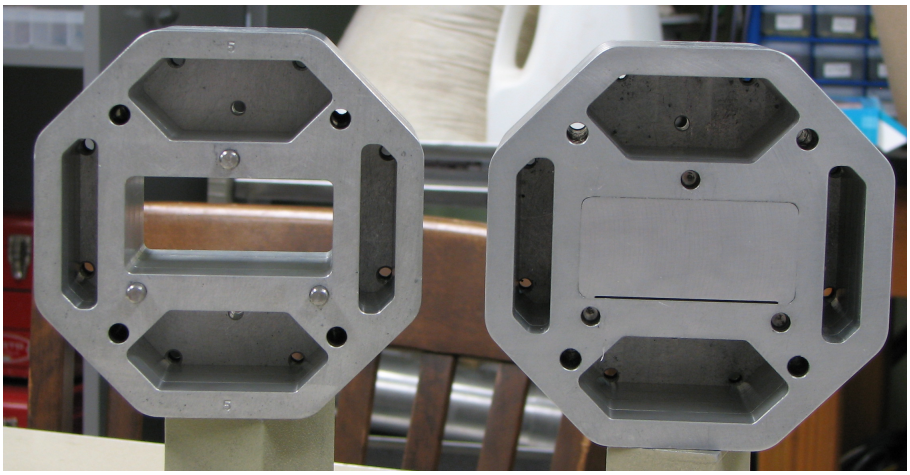

Figure 2.2: Outer and ENZ rectangular waveguides

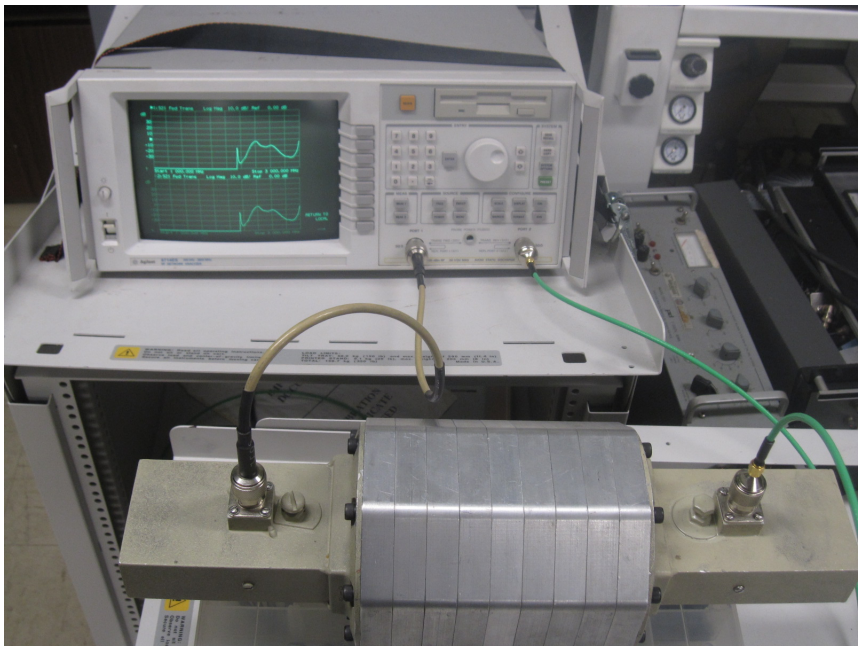

Figure 2.3: Measurements with vector network analyzer

2.1.3 Measured results

The data acquisition/post-processing system is implemented using National Instruments LabVIEW virtual instruments and with a connection through

Figure 2.4: ENZ experimental setup with National Instruments data acquisition

a general-purpose interface bus (GPIB) interface. Figure 2.5 shows the LabVIEW GUI that programs and collects the experimental data; in the figure, S22 is shown. Measurements of the scattering parameters were taken and compared to full-wave simulations of the setup shown in figure 2.3. In figure 2.6, the measurements agree well to the simulation, but the characteristics of the waveguide-to-coax transitions were not considered, which lead to non-idealities shown in figures 2.5 and 2.6. First, as can be seen in Fig. 2.5, the reference

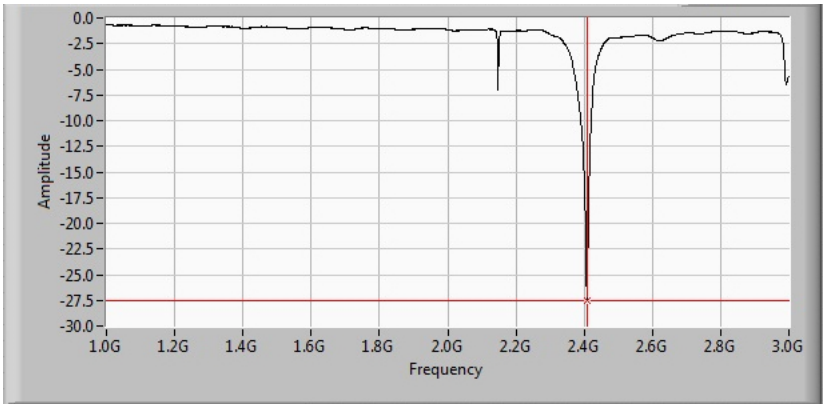

Figure 2.5: LabVIEW front panel displaying S22 of the experimental setup

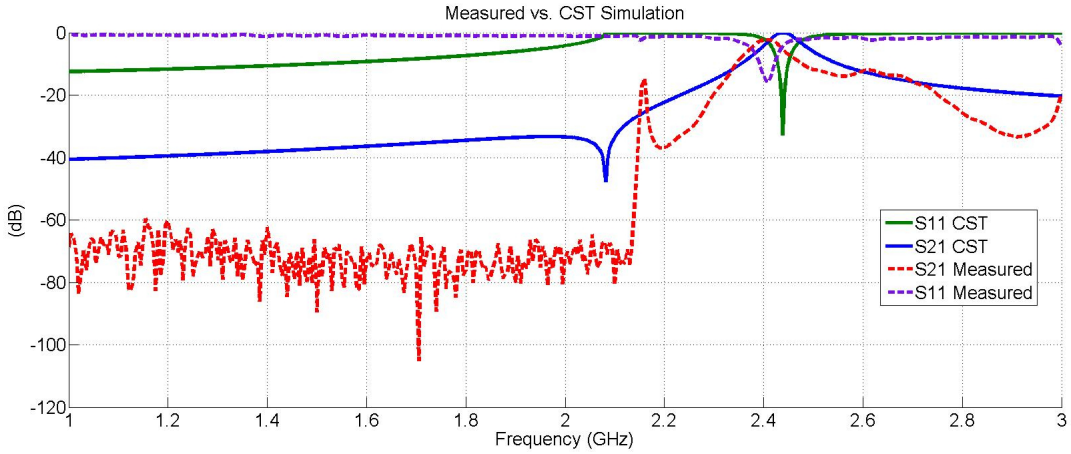

Figure 2.6: Measured versus simulated scattering parameters

0 dB level is off, which is due to the lack of initial calibration. Calibrating waveguides is non-trivial without proper standards, but the the lack of calibration does not affect the overall supercoupling phenomenon, which is clearly seen around the cutoff frequency of the inner waveguide section ($f_c^{ENZ} = 2.46$ GHz). The other relevant non-ideality is the other small resonance close to 2.15 GHz. This other resonance is due to the cutoff of the waveguide-to-coax

transitions used to excite the experimental setup in figures 2.3 and 2.4 and not the device under study (DUT). To explain the waveguide transition effects further, the same numerical data was compared against a simulation of the experimental setup excluding calibration.

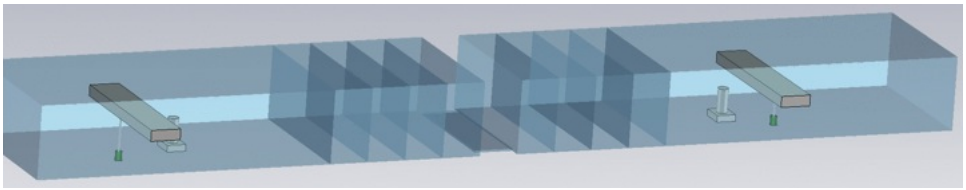

Figure 2.7: CST simulation of PEC experimental setup

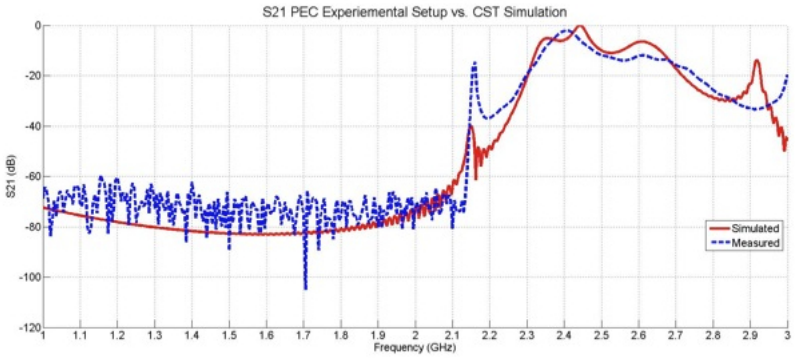

Figure 2.8: S21 of PEC experimental setup

The full experimental simulation was done using PEC and aluminum structures and is shown in Fig. 2.7. The effects of loss were shown to be marginal as anticipated, and a comparison between the PEC and aluminum cases are shown in figures 2.8 and 2.9. The same data from Fig. 2.6 were used to evaluate the differences between the waveguide transition and no transition cases. The waveguide-to-coax transitions were physically measured and

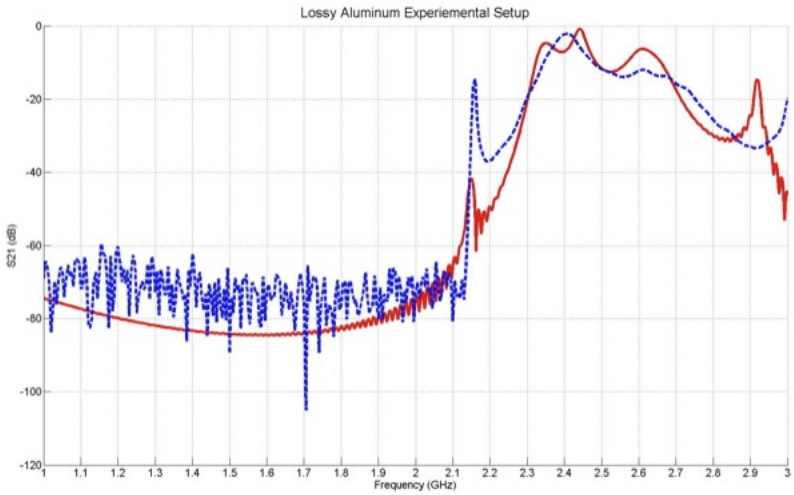

Figure 2.9: Transmission of aluminum experimental setup

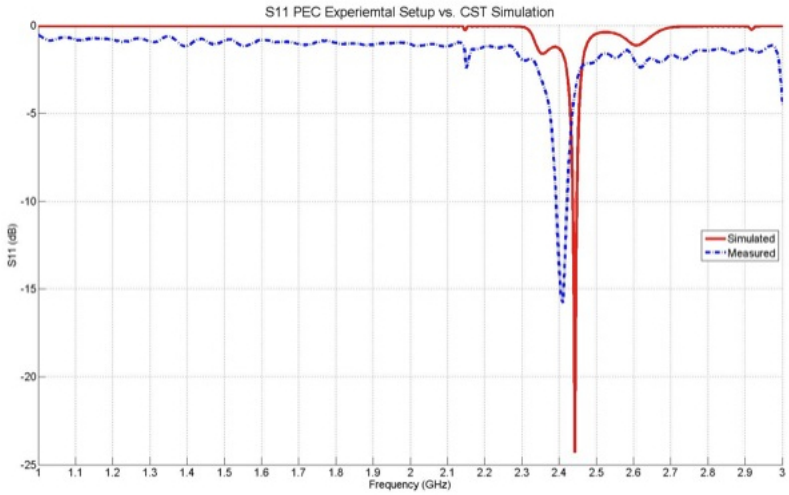

Figure 2.10: S11 of PEC experimental setup simulation versus experimental data

simulated to best resemble the HP8714ES VNA output. These measurements were prone to error, since no datasheet exits for them. The minor discrepancies are most likely due to inaccuracies in the physical measurements of the

waveguide-to-coax transitions.

However, these simulations give us an indication of the contribution of the transitions to the overall measurements. The general trend between the simulation and experimental data of the transmission and reflection in figures 2.10, 2.9, and 2.10 is very similar. We can clearly see that the measured and simulated show the cutoff of experimental system occurs slightly after the cutoff of the outer waveguide transitions, and this is evidenced by the large transmission discontinuity and resonance around 2.15 GHz in figures 2.9 and 2.10. The cutoff of the outer waveguide is ideally $f_c^{out} = 2.08$ GHz. Since there is no E-plane discontinuity between the waveguide transition and the outer waveguide section, the resonant frequency is moved slightly up to about 2.15 GHz. Therefore, the transitions have moved the overall cutoff up in frequency, which must be due to an equivalent inductive load introduced by the transitions. A mode-matching analysis of the waveguide transitions could be used to verify this.

2.2 ENZ Frequency Stability and Bandwidth

The reflection scattering parameters comparing one and two ENZ phase plates for the experimental setup and are given in figure 2.11. In this study, we took measurements of one ENZ plate versus two ENZ plates. An important aspect of this study is that the bandwidth decreases as the ENZ channel length increases. This is due to the junction reactive loading at the discontinuities. Since the channel is shorter, the evanescent modes are more apparent. This

is in full agreement with simulation and the channel length variation in the experiments done in [16, 17]. This relationship is best shown in the extreme case of the 180° ENZ bend in [17].

Another very interesting and important fact is that the ENZ frequency is constant independent of the ENZ channel length for this two-plate study. However, as the ENZ channel becomes longer, the waveguide transition cutoff frequency becomes more apparent as can be seen in Fig. 2.11. While it is not shown in this study, we can be assured that a Fabry-Perot resonance will also come into the operating bandwidth as the ENZ channel length becomes longer.

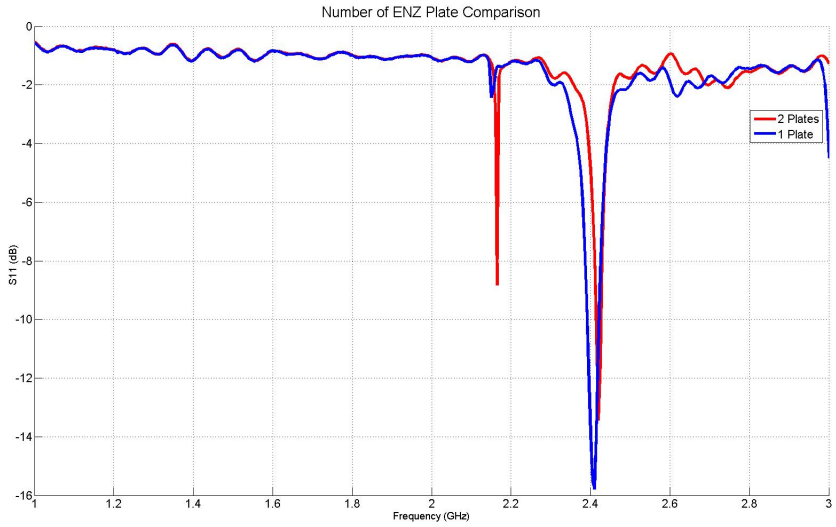

Figure 2.11: Measured S11 of experimental setup for 1 vs. 2 ENZ phase plates

Chapter 3

Antenna Design Using Epsilon-Near-Zero Metamaterials

3.1 The Reciprocal Problem

The waveguide supertunneling effect was derived and verified in Chapters 1 and 2. We showed through simulation and experimental measurement, as well as the excellent independent work provided in [16, 17, 18], that this tunneling is a new physical phenomenon, which is unique and quite different from Fabry-Perot resonances. The experimental verification with rectangular waveguides also showed that this kind of metamaterial does not rely on complex inclusions, as is the usual case for metamaterials, but can be implemented by using the frequency dispersion of a rectangular waveguide at cutoff, which provides an epsilon-near-zero cavity.

In this chapter, we will show that a semi-rigid 50 Ω coaxial cable can be matched to the ENZ device regardless of its longitudinal position. This demonstrates the "static" properties of the enhanced electric field through the ENZ channel. This unique matching concept offers a new degree of freedom for the engineer. Primarily, this new matching technique allows matching to antennas and waveguides regardless of the shape or discontinuities of the

antenna or waveguide structure. This independance upon length, shape, or discontinuity is due to the infinite phase velocity of the wave in the ENZ cavity. Therefore, the impinging wave does not even "see" the cavity and instantly travels to the connecting structure as if the cavity was not there at all. The works of [12], [14], [15], [16], and [17] have rigorously derived and verified the matching of arbitrary bends and discontinuities.

We will also introduce a multi-band antenna and use cylindrical transmission lines to characterize its behavior for an ENZ gap launching antenna. There will be several investigations, beginning with an understanding of a radiating post loaded with ENZ gaps. Next, we will investigate how the geometry affects critical parameters such as the coaxial-matching and antenna bandwidth. Then work will be carried out on how to optimize these parameters. The approaches from Chapter 1 and 2 will be used to re-discover the physics and analytical models that describe these new structures.

3.2 Waveguide-to-Coax Matching Using an ENZ Cavity

3.2.1 Transverse coaxial match

Up to this point, this and previous works have demonstrated that an electromagnetic wave can be coupled through an extremely tight entrance. This tunneling was shown to occur because the reflection coefficient at the entrance went to zero as the height of the entrance of the ENZ channel became vanishingly small [12], [13], [14]. Due to the drastic geometric differences at the interface, the outer electromagnetic wave will have a very different wave

impedance than that of the wave in the ENZ channel. However, the smallness of the ENZ entrance and the effective permittivity near zero will effectively compensate for each other to match the outer waveguide to the ultra-narrow ENZ cavity.

In this section, we will continue the work by Alú [15]. We will show that a coaxial cable can be matched very well to outer waveguides and antenna structures through an ENZ channel. The use of an ENZ channel for matching provides several benefits over other methods of waveguide and antenna matching. The ENZ matching technique allows matching to arbitrarily shaped structures, which could lend itself very well to the size reduction of energy transmission systems as well as conformal structures. Additionally, the matching of a coaxial cable by an ENZ channel is highly independent of its longitudinal position, which gives the engineer an extra degree of freedom in matching waveguides and antennas.

Figure 2.1 shows is the same experimental setup under study in this section. In this arrangement, we will use the properties of the ENZ rectangular waveguide at cutoff to match a standard 50 Ω coaxial cable to the outer waveguides. Work previously done by Alú [15] showed that a coaxial cable can be matched to an antenna or waveguide structure by using the frequency dispersive characteristics of a rectangular waveguide at cutoff. In his work, Alú demonstrated that a matching condition exists for drastically different wave impedances using the asymptotic characteristic of the channel impedance near cutoff.

The epsilon-near-zero compensation was shown in Equations 1.4 and 1.5, but can be written in another form that shows the explicit compensation by the effective ENZ permittivity. Equations 3.1 and 3.2 show that the large difference in waveguide heights, a and a_{ch}, is compensated near an effective permittivity of zero, rather than exactly at $\epsilon = 0$. While it may seem counter-intuitive that the matching becomes better as the ENZ entrance is reduced, since this should lead to an electrical short circuit with Γ = -1, the matching is due to voltage continuity across each of the waveguides. The voltage continuity shows that the reduction of the ENZ channel actually works to counteract the infiniteness of the waveguide at cutoff. Therefore, over a small region of bandwidth, the outer waveguide and the ENZ channel are matched.

$$Z_{ENZ} = \frac{a_{ch}}{w_{ch}} \sqrt{\frac{\mu_0}{\epsilon_{eff}^{ch}}} \tag{3.1}$$

$$Z_{OUT} = \frac{a}{w} \sqrt{\frac{\mu_0}{\epsilon_{eff}^{out}}} \tag{3.2}$$

The ideal matching for the setup in Fig. 2.1 is shown in Fig. 3.1. In this construction, the wave is free to tunnel through the channel due to ENZ match about cutoff. Moreover, the coax will see one half the wave impedance of the outer waveguide sections, since the waveguides are in parallel. This phenomenon is given in equation 3.3.

$$Z_0^{match} = \eta_0^{out} || \eta_0^{out} = \frac{\mu_0 \omega}{2\beta_{10}^{out}} \tag{3.3}$$

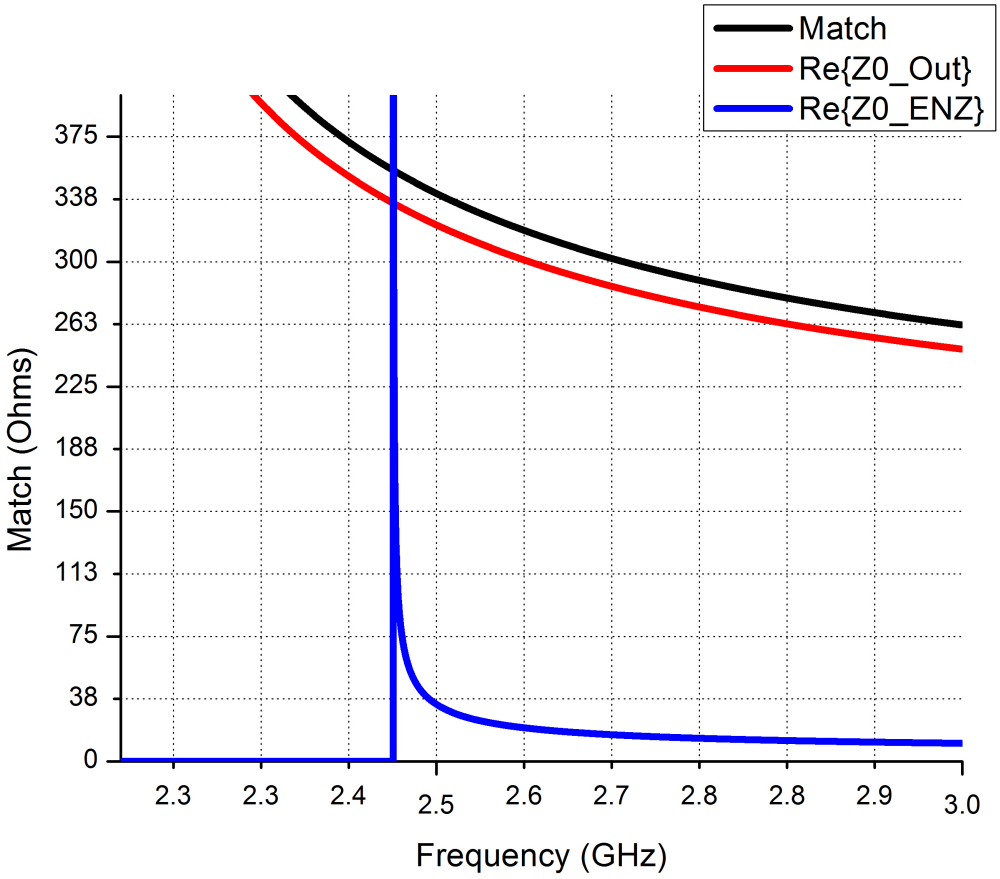

Figure 3.1: Matching the ENZ channel to the outer waveguides at cutoff.

Figures 3.1 and 3.2 demonstrate the ENZ matching condition. In the ENZ cavity, ϵ_{eff} is zero at cutoff; therefore, $Z_{0,ch}$ is infinite at the cutoff of the connecting rectangular waveguide. This asymptotic impedance crosses the outer waveguide impedance very sharply, and at this point, the supertunneling effect occurs. At this point the matching impedance is given by the curve "Match" in Fig. 3.1. What's more, while the cutoff impedance is asymptotic,

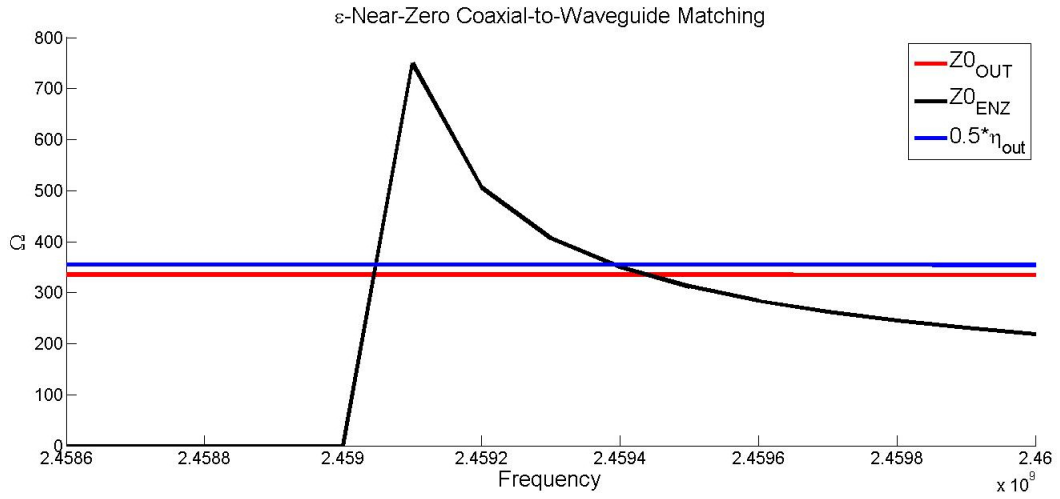

Figure 3.2: ϵ-near-zero coaxial matching

the compensation due to the ENZ occurs more broadly than exactly at $\epsilon = 0$.

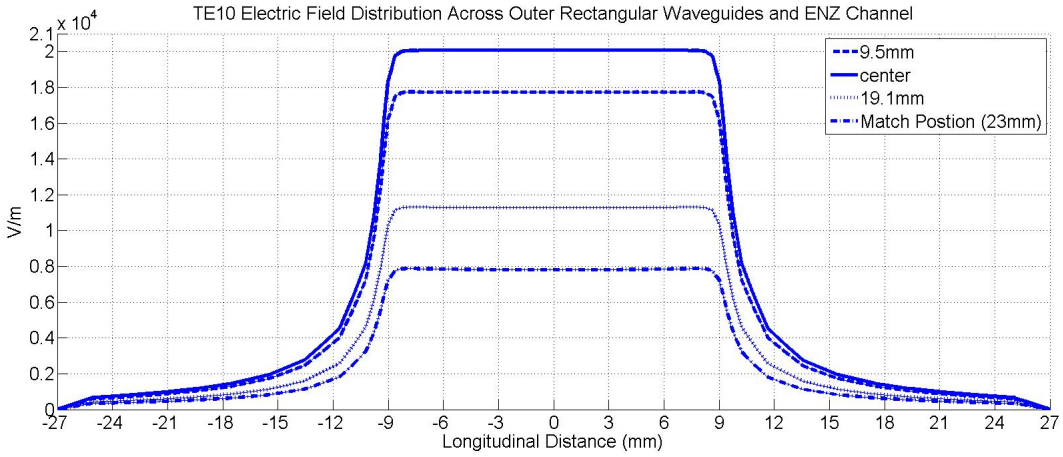

Figure 3.3: Electric field amplitude across waveguide-to-coaxial experiment for different transverse positions

The models shown in figure 3.1 assumes the maximum electric field in the middle of the ENZ channel. Since the field is TE_{10}, the field decreases

monotonically from the middle of the cavity to zero at the edges. Therefore, a way to match a standard cable to the waveguide is by moving the coaxial cable in the transverse direction. Additionally, since the field is *static-like* in the propagating direction, moving the cable longitudinally will have no effect on the coaxial match. These results were predicted in Chapter 1 and demonstrated in figure 3.3.

Figures 2.1 shows the placement of the type -141, 50 Ω, standard rigid connector. The transverse electric field magnitude is plotted as a function cavity position in figure 3.3. It can be seen that the electric field has substantial amplitude enhancement in the ENZ channel and is constant in phase as predicted in Chapter 1. As can be seen in Fig. 3.3, a transverse position at 23 mm from the center of the ENZ waveguide was chosen to match the -141 coaxial cable, and the S11 and S21 for this match are shown in Fig. 3.4.

3.2.2 Longitudinal matching independence

To further show the longitudinal matching independence, Fig. 3.5 was simulated. As can be seen in the figure, there are five ENZ phase slots with one of them connected to the -141 50 Ω cable. The cable was moved several times to see the effects on the matching. First, a study was done on the effects of the length of the channel on the matching frequency and the corresponding return loss and fractional bandwidth (FBW); this is shown in figures 3.6 and 3.7. Then the coaxial cable was moved to each of the five slots, and the matching was evaluated again; this is shown in Fig. 3.8.

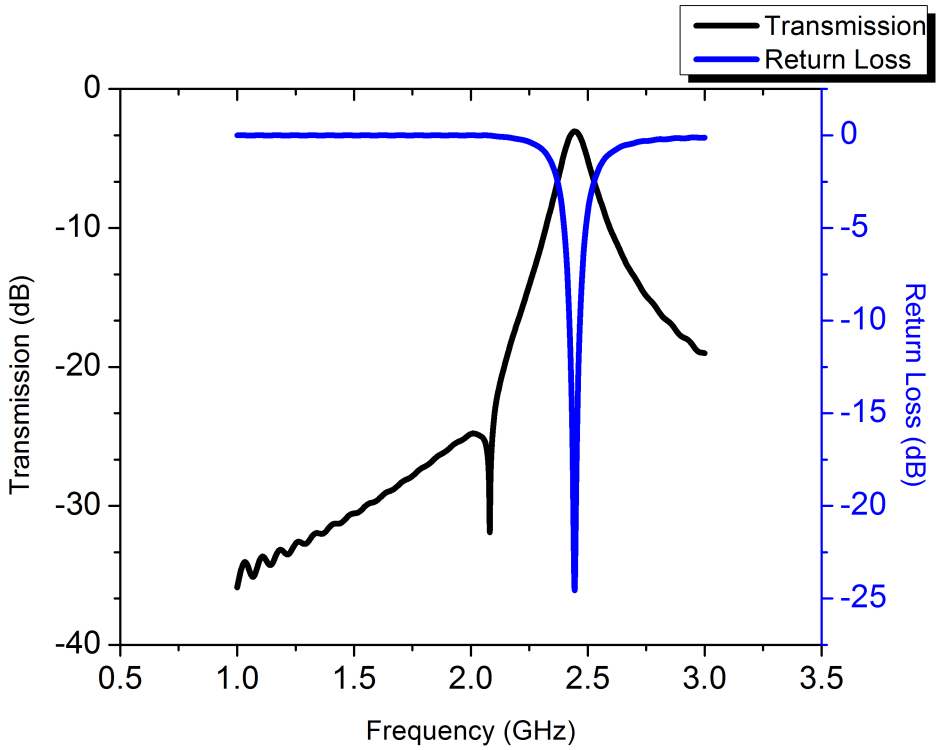

Figure 3.4: Return loss and transmission of coaxial match at 23 mm from the center in the ENZ channel

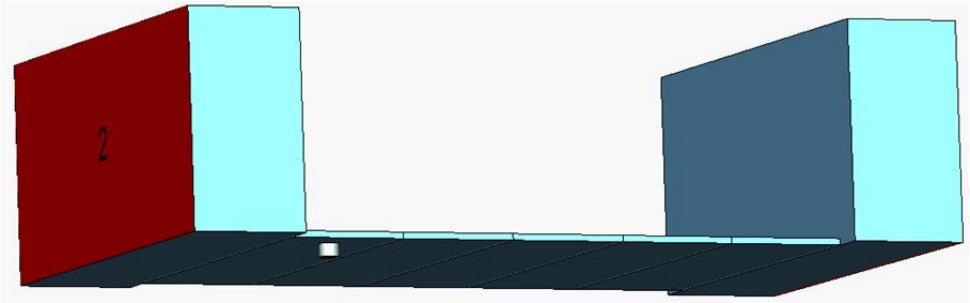

Figure 3.5: Coaxial matching longitudinal independence simulation

Figure 3.8 evaluates the matching and return loss for the -141 coaxial cable at each of the five phase plates at the same transverse position. Since the

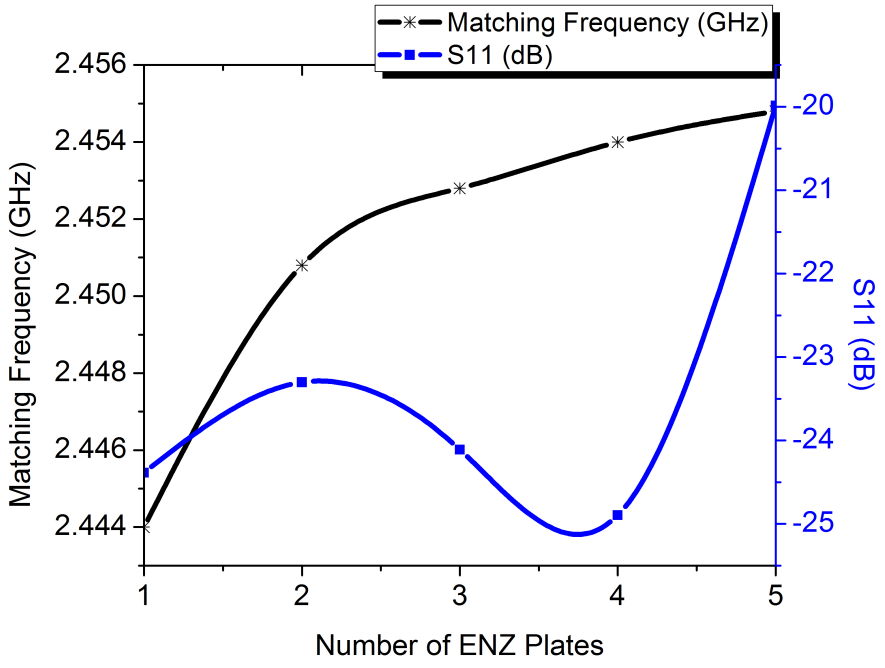

Figure 3.6: Matching frequency and return loss versus number of plates

waveguide section is reciprocal, only slots 1, 2, and 3 are necessary, but Fig. 3.8 verifies this fact. In the figure, the matching varies by less than 0.016%, and the return loss varies by 3.0%.

Figures 3.6 through 3.8 prove the matching is essentially unchanged by moving the coaxial cable longitudinally. One key observation in Fig. 3.7 is the FBW is affected by the length of the ENZ channel due to lower loading of the reactive fields at the ENZ-waveguide interfaces.

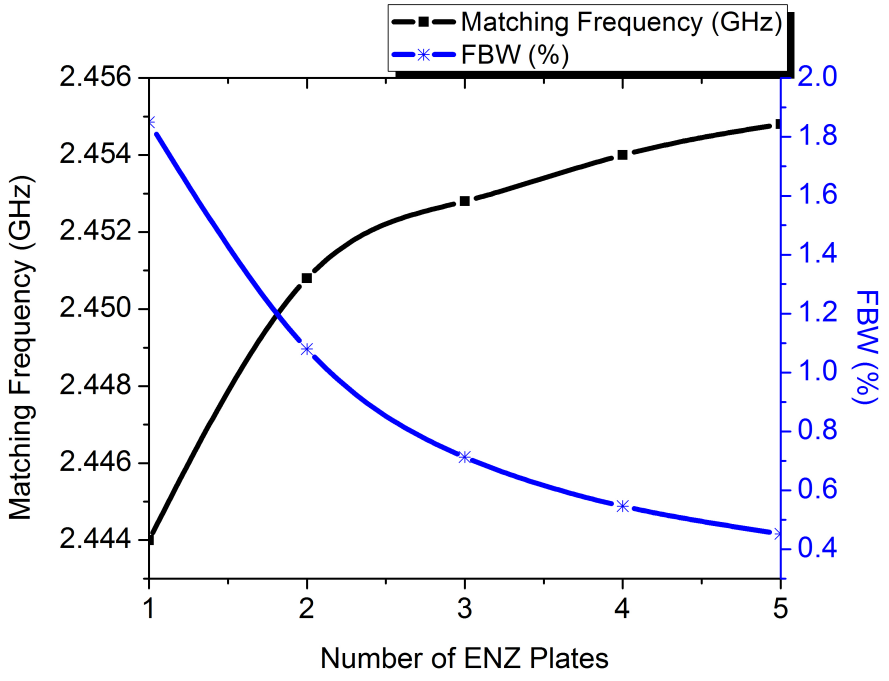

Figure 3.7: Fractional bandwidth versus number of ENZ plates

3.3 ENZ Pyramidal Horn Antenna

In the previous sections, we have shown that a standard coaxial cable can be matched to two rectangular waveguide horns and a radial waveguide. Therefore, reciprocity does indeed hold for the energy tunneling ENZ concept. To further develop this concept, we will next show the ENZ cavity can be used as a matching element for an antenna structure. First we will show the matching and far-field characteristics for a single-channel horn antenna, then we will apply the ENZ tunneling concept to a multi-channel horn and radial waveguide antenna. These studies will also show two different methods of creating an ENZ cavity that can be used in practical antenna applications.

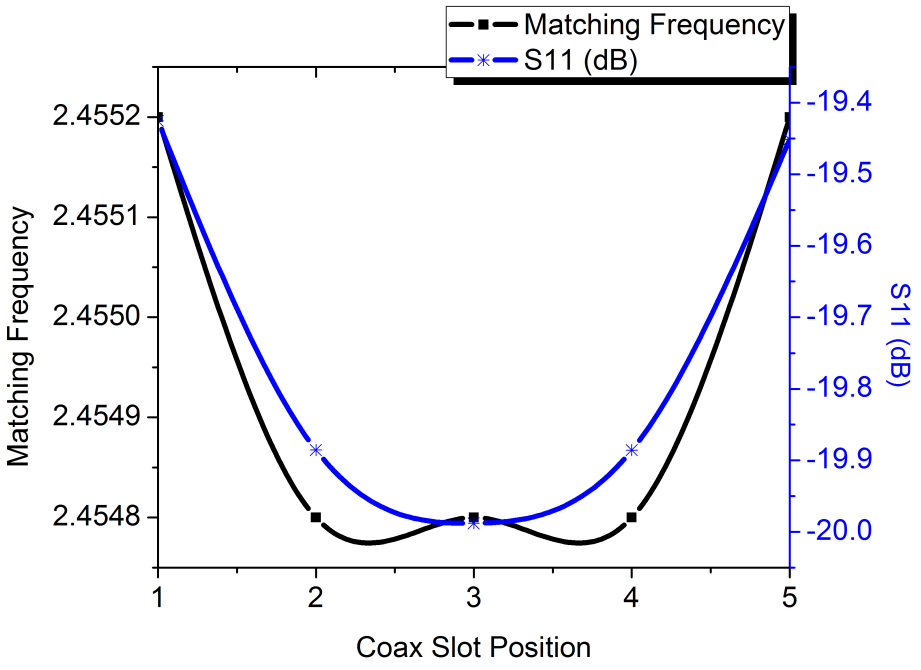

Figure 3.8: Coaxial matching longitudinal independence

3.3.1 Single-channel rectangular horn antenna

A pyramidal horn is shown in Fig. 3.9, which is matched through an ENZ cavity. The ENZ cavity is implemented with an air-filed rectangular waveguide at cutoff. The ENZ cavity was designed to have a cutoff at 1.5 GHz, and with dimensions $a_{ch} = 1$ mm, $w_{ch} = 100$ mm, and $l_{ch} = 25$ mm, as in Fig. 1.2. The dimensions of the outer rectangular waveguide and pyramidal horn are w = 150 mm, a = 40 mm, A = 260 mm, B = 370 mm, and a taper angle of 30 °.

The pyramidal horn was used since it is one of the most common horn antennas in use, and directivities are generally between 10 to 20 dBi from

standard manufacturers. The goal of using this structure is to show that an ENZ cavity can match a coaxial cable very well for standard horn antennas with good matching bandwidth (FBW), half-power bandwidth (HPBW), side lobe level (SLL), and directivity (DIR) properties.

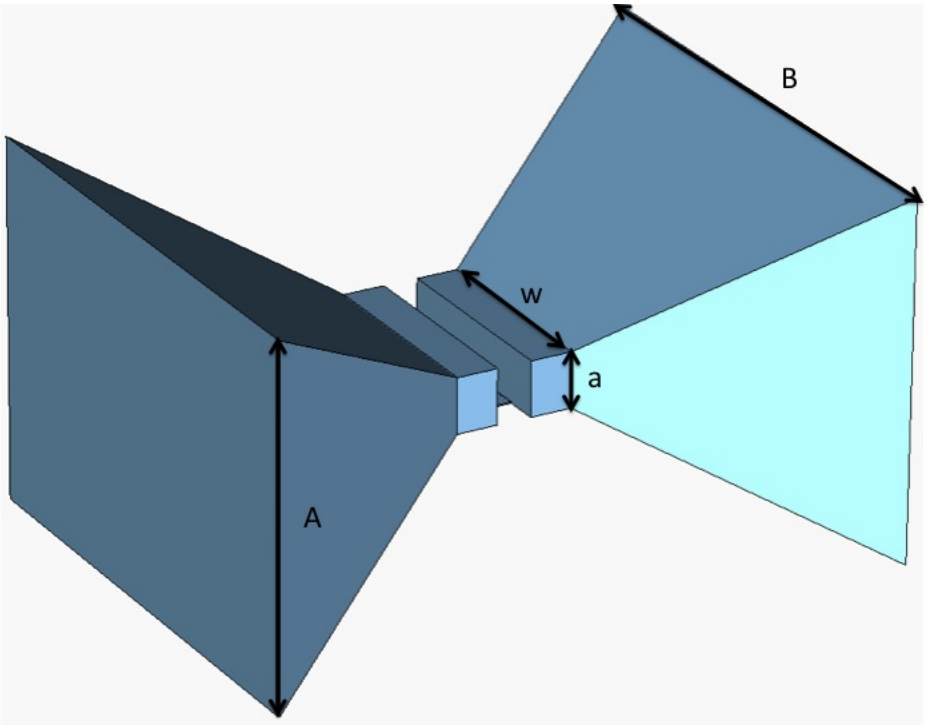

Figure 3.9: Pyramidal horn antenna used with an ENZ matching cavity.

Figure 3.10 shows the far-field pattern for the antenna in Fig. 3.9. The performance characteristics are given in Table 3.1. The performance shown in Table 3.1 is very respectable and shows that an ENZ cavity works well as a matching device to an antenna as well as the previously shown waveguide structures.

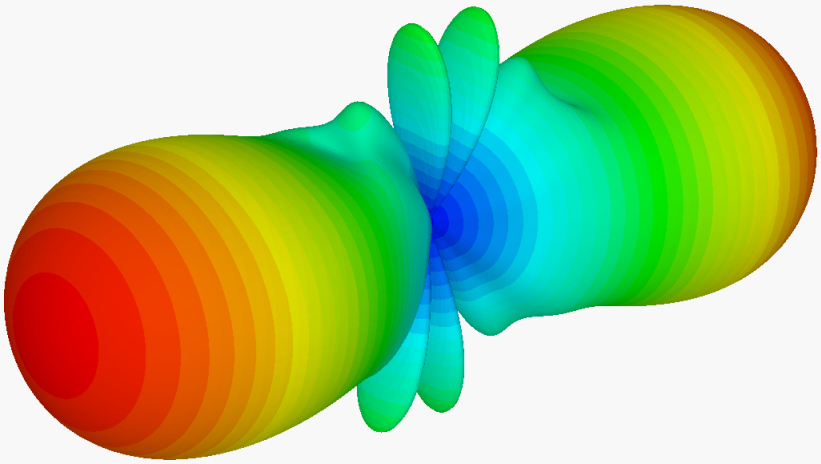

Figure 3.10: Pyramidal far-field pattern

Table 3.1: Ideal pyramidal horn antenna performance

	E-Plane	H-Plane
DIR (dBi)	10.7	10.7
SLL (dB)	-11.2	-25.2
HPBW (degrees)	37.7	40.2
Match Frequency (GHz)	1.49	1.49
Match Resistance (Ω)	159	159
FBW (%)	10.4	10.4

The antenna in Fig. 3.9 was studied for its matching frequency stability, matching input resistance, and directivity. These studies are shown in figures 3.11 and 3.12, respectively. These studies show that the matching frequency is very stable over the horn length, but the matching resistance oscillates between 190 and 150 Ω, obviously since the phase of the fields inside the horns are non-static. In Fig. 3.12, we can see the directivity increases by lengthening the horn, which implicitly increases the outer horn aperture and provides a longer

taper to match the rectangular waveguide impedance to free space. There are well-known methods to optimize the gain of a horn, but in this case, the performance of the designed antenna is a very good proof-of-concept.

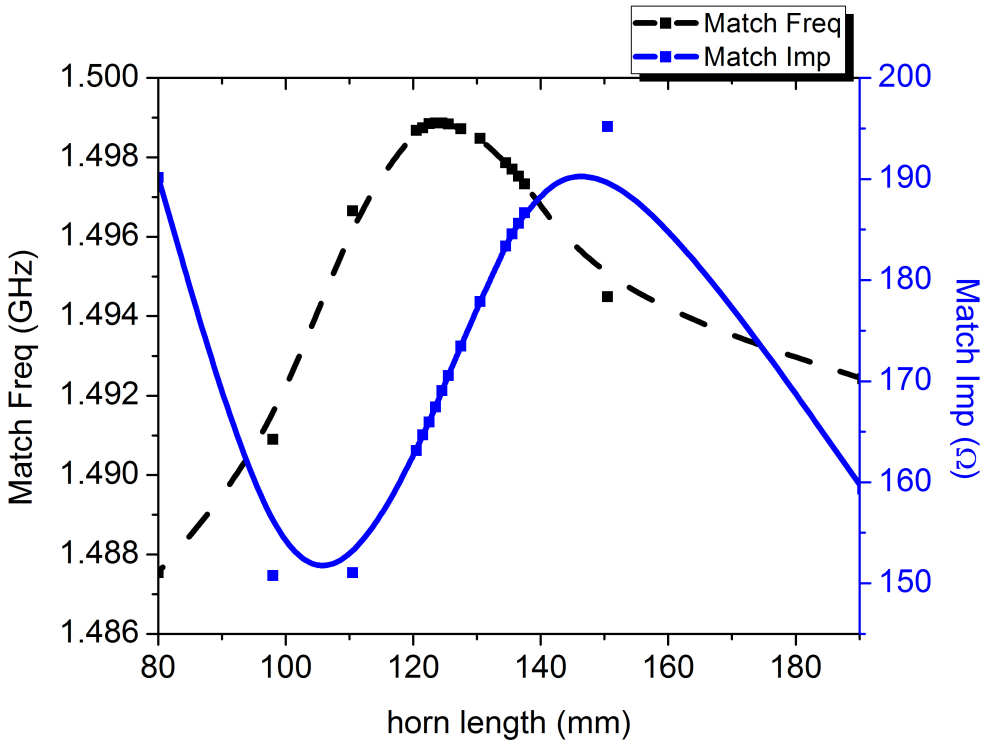

Figure 3.11: Matching frequency and resistance versus horn length

Just as was done for the rectangular waveguide case in the beginning of this chapter, we wish to match the pyramidal ENZ horn antenna to a standard 50 Ω coaxial cable. As has been shown, the matching resistance of the *center* of the ENZ cavity is 159 Ω; however, we can use the half-wavelength symmetry of the TE_{10} mode to match to a lower input resistance. A standard -141 coaxial cable was used with the dimensions $d_{conductor} = 0.91$ mm and $d_{dielectric}$

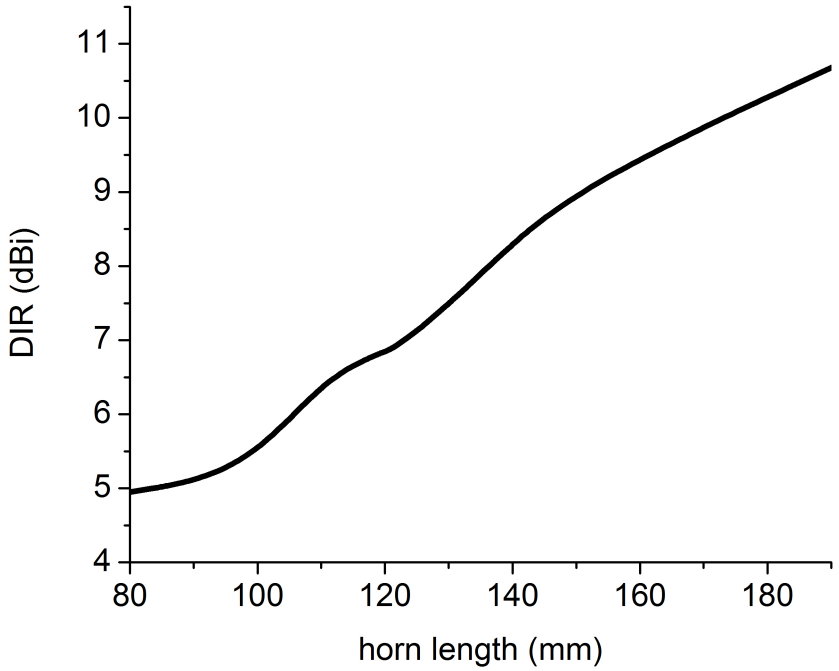

Figure 3.12: Directivity versus horn length

= 2.98 mm, and with a dielectric filling of Teflon (ϵ_r = 2.1). Figure 3.13 shows the optimized coaxial position attached to the ENZ cavity. Figure 3.14 demonstrates the variation of the matching frequency and S11 for a given coax position on the ENZ cavity. The positions given in Fig. 3.14 are measured as an offset from the center; i.e., position 0 means the center of the ENZ cavity. The optimized position was found to be 39 mm from the center of the ENZ channel, which gave an S11 better than -30 dB and matched at 1.5 GHz, as designed for.

Table 3.2 is a summary of the same parameters that were given in Table

3.1. The parameters stayed basically the same, but with a slightly better FBW.

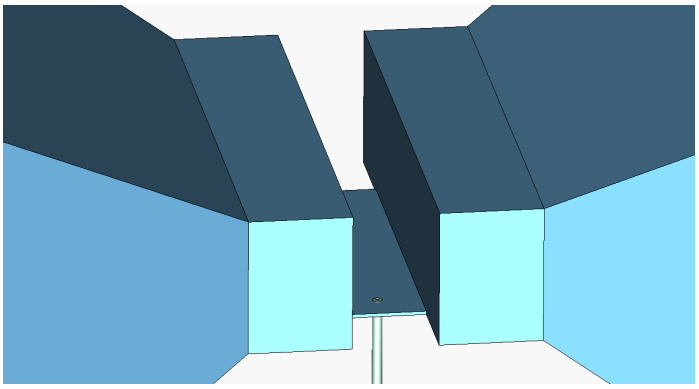

Figure 3.13: Off-center -141 coaxial match to the horn antenna

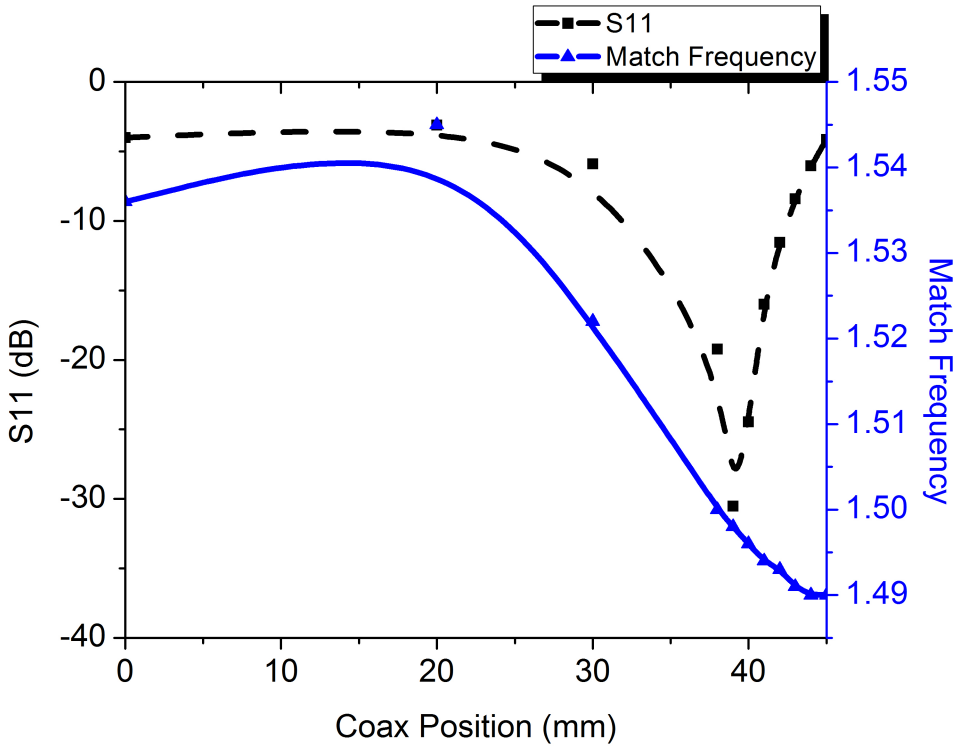

Figure 3.14: Matching frequency and S11 across ENZ cavity

Table 3.2: Coax-matched pyramidal horn antenna performance

	E-Plane	H-Plane
DIR (dBi)	10.7	10.7
SLL (dB)	-11	-25.4
HPBW (degrees)	38	40.7
Match Frequency (GHz)	1.498	1.498
Match Resistance (Ω)	50	50
FBW (%)	11.2	11.2

3.3.2 Multi-band pyramidal horn ENZ antenna

Figure 3.15 shows a three-channel pyramidal horn antenna with the same dimensions as Fig. 3.9. However, now two extra channels have been implemented as rectangular waveguides at cutoff. The dimensions are $w_{ch,top}$ = 140 mm, $w_{ch,mid}$ = 80 mm, and $w_{ch,bottom}$ = 100 mm, which corresponds to resonant frequencies of 1.07, 1.875, and 1.5 GHz, respectively. For the ideal case, with infinitesimal waveguide excitations, the three-channel antenna has excellent matching performance and far-field patterns. Antenna characteristics for each of these gap launchers are reported in Tables 3.3, 3.5, and 3.4. This shows that an ENZ channel can be designed very easily using rectangular waveguides at cutoff to match coaxial cables to an antenna structure as well as to waveguides. As can be seen in Tables 3.3, 3.4, and 3.5, almost every important aspect of antenna performance is excellent using this new antenna matching scheme.

We can modify the antenna of Fig. 3.15 to create a quad-directional pyramidal horn antenna. This antenna is shown in Fig. 3.19. In this configu-

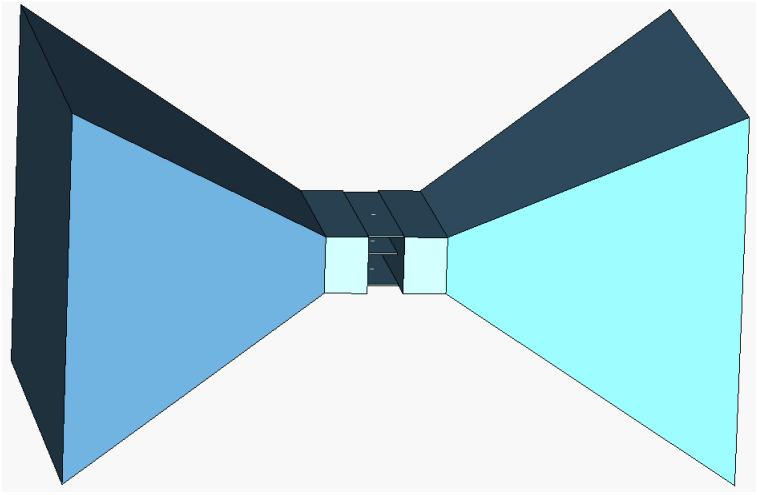

Figure 3.15: Triple-band pyramidal ENZ horn antenna

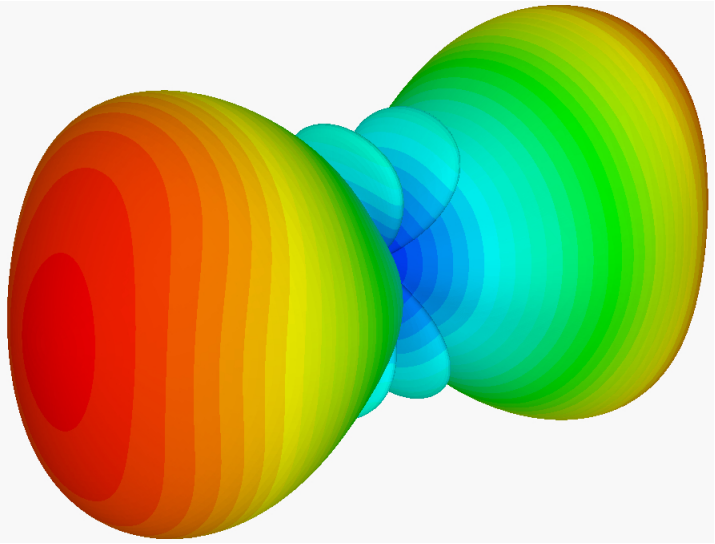

Figure 3.16: Low frequency channel far-field pattern

ration, we can send three different frequency bands in four different directions, which could be useful in a point-to-point station. The radiation patterns of each of the three channels is given in figures 3.20–3.22 and exhibits excellent

Table 3.3: Ideal low frequency channel antenna performance

	E-Plane	H-Plane
DIR (dBi)	6.68	6.68
SLL (dB)	-9.5	-16.5
HPBW (degrees)	75.3	57.3
Match Frequency (GHz)	1.07	1.07
Match Resistance (Ω)	235	235
FBW (%)	6.7	6.7

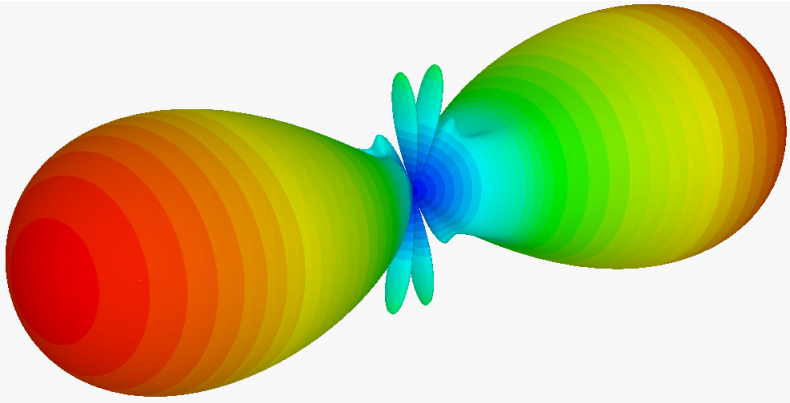

Figure 3.17: Middle frequency channel far-field pattern

Table 3.4: Ideal mid frequency channel antenna performance

	E-Plane	H-Plane
DIR (dBi)	10.7	10.7
SLL (dB)	-11.2	-25.2
HPBW (degrees)	37.6	40.2
Match Frequency (GHz)	1.49	1.49
Match Resistance (Ω)	160	160
FBW (%)	10.3	10.3

radiation at the designed frequency bands. The issues of this antenna structure are very high matching resistance and is very narrow-bandwidth performance.

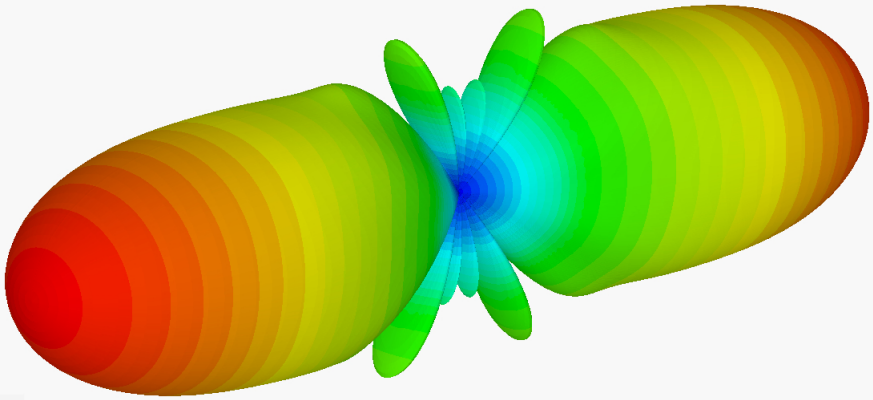

Figure 3.18: High frequency channel far-field pattern

Table 3.5: Ideal high frequency channel antenna performance

	E-Plane	H-Plane
DIR (dBi)	10.7	10.7
SLL (dB)	-9.9	-21.7
HPBW (degrees)	28.4	29.8
Match Frequency (GHz)	1.49	1.49
Match Resistance (Ω)	207	207
FBW (%)	8.3	8.3

Additionally, while the directivities are still very desirable, they are slightly reduced from the structure in Fig. 3.15. The reasons for these drawbacks are due to the increased coupling by attaching a second quadrature ENZ waveguide with the original single ENZ waveguide. As was shown in previous sections, the reduced bandwidth is mainly due to the lengthening of the channel lengths in order to fit the horns together in this configuration. Therefore, the pyramidal horn antenna in Fig. 3.15 is a better performing and more practical antenna implementation to the ENZ matching technique.

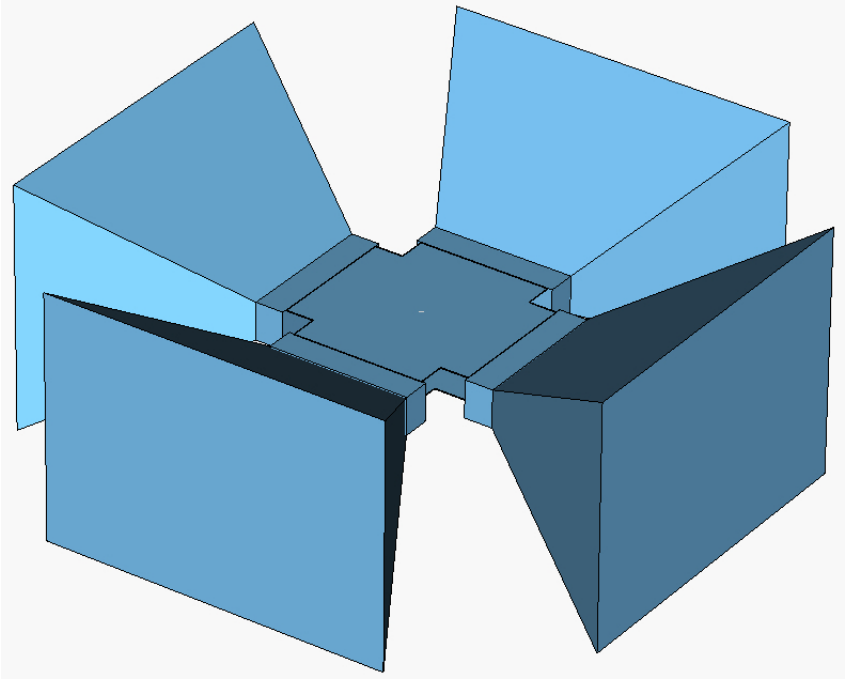

Figure 3.19: Quadrature pyramidal ENZ horn antenna

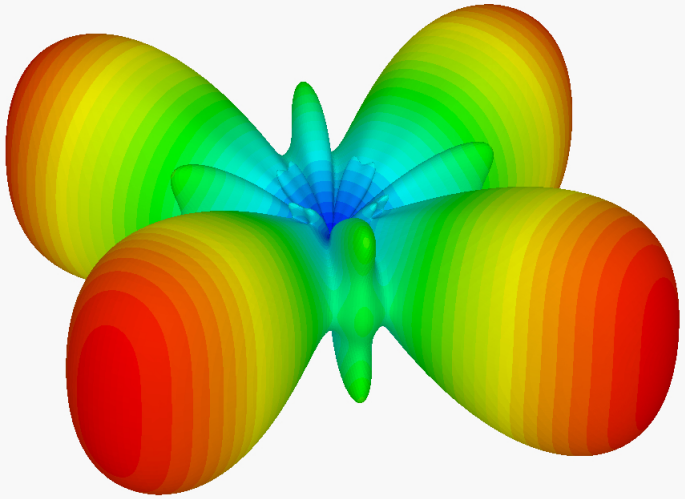

Figure 3.20: Low-band of the quadrature pyramidal ENZ horn antenna

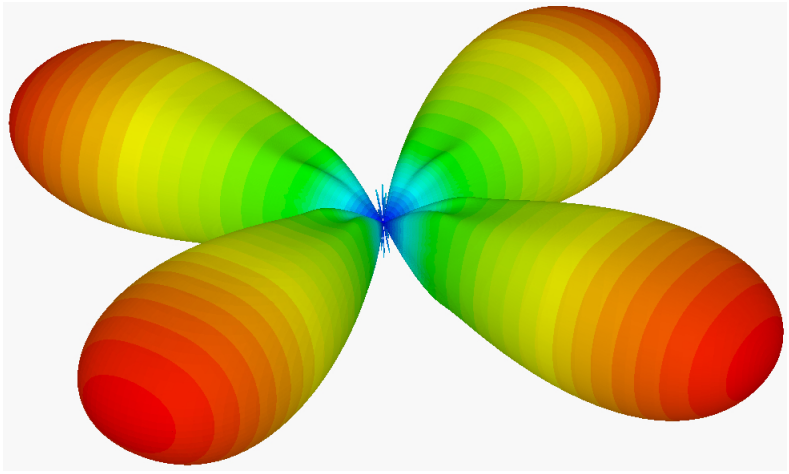

Figure 3.21: Mid-band of the quadrature pyramidal ENZ horn antenna

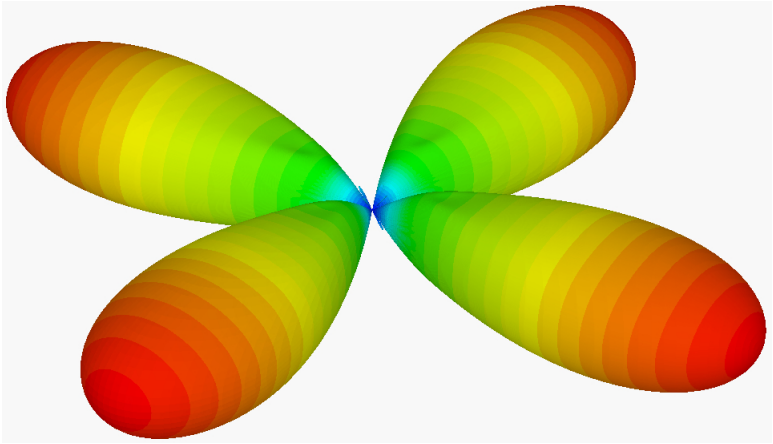

Figure 3.22: High-band of the quadrature pyramidal ENZ horn antenna

3.4 Cylindrical Transmission Lines

Now we will apply the reciprocity theorem to a radial waveguide and show that coaxial matching can be applied equally well to geometries other than parallel-plate and rectangular waveguides. We will further show that the ENZ matching can be successfully applied to antennas.

A transmission line can be defined for the radial waveguide since there is indeed a TEM mode, but the geometry of the system will augment the fields due to scattering. Starting from the Maxwell equations for a source-free, linear, and isotropic medium, the seperation into each of the components is not quite as straight-forward as the decoupling of the components in the Cartiesian system [19], [20] and [21]. The general outwardly radial fields are represented in equations 3.4 through 3.10.

$$E_{\rho}^{+} = jB_{mn}\beta_{\rho}\frac{n\pi}{h\omega\mu\epsilon}\frac{\partial H_{m}^{(2)}\left(\beta_{\rho}\rho\right)}{\partial\left(\beta_{\rho}\rho\right)}\cos\left(m\phi\right)\sin\left(\frac{n\pi z}{h}\right) \tag{3.4}$$

$$E_{\phi}^{+} = -jB_{mn}\frac{mn\pi}{h\omega\mu\epsilon\rho}H_{m}^{(2)}\left(\beta_{\rho}\rho\right)\sin\left(m\phi\right)\sin\left(\frac{n\pi z}{h}\right) \tag{3.5}$$

$$E_{z}^{+} = -jB_{mn}\frac{\beta_{\rho}^{2}}{\omega\mu\epsilon}H_{m}^{(2)}\left(\beta_{\rho}\rho\right)\cos\left(m\phi\right)\cos\left(\frac{n\pi z}{h}\right) \tag{3.6}$$

$$H_{\rho}^{+} = -B_{mn}\frac{m}{\mu\rho}H_{m}^{(2)}\left(\beta_{\rho}\rho\right)\sin\left(m\phi\right)\cos\left(\frac{n\pi z}{h}\right) \tag{3.7}$$

$$H_{\phi}^{+} = \frac{-\beta_{\rho}B_{mn}}{\mu}\frac{\partial H_{m}^{(2)}\left(\beta_{\rho}\rho\right)}{\partial\left(\beta_{\rho}\rho\right)}\cos\left(m\phi\right)\cos\left(\frac{n\pi z}{h}\right) \tag{3.8}$$

$$H_{z}^{+} = 0 \tag{3.9}$$

$$\beta_{\rho} = \sqrt{\beta^{2} - \left(\frac{n\pi}{h}\right)^{2}} \tag{3.10}$$

These equations represent the outward-traveling radial waves in an infinite parallel-plate waveguide with a cylindrical post as the source. Here, h represents the distance separating the two plates and strongly affects the cut-off of the waveguide for higher-order modes. Starting from the general field equations in 3.4 through 3.10, the TEM case can be investigated by setting m = n = 0. This results in intuitive and satisfying results.

$$E_\rho^+ = E_\phi^+ = H_\rho^+ = H_z^+ = 0 \tag{3.11}$$

$$E_z^+ = -j\omega B_{00} H_0^{(2)}(\beta\rho) \tag{3.12}$$

$$H_\phi^+ = \frac{-\omega B_{00}}{\eta} \frac{\partial H_0^{(2)}(\beta\rho)}{\partial(\beta\rho)} = \frac{\omega}{\eta} B_{00} H_1^{(2)}(\beta\rho) \tag{3.13}$$

$$\beta_\rho = \beta = \frac{\omega\sqrt{\epsilon_r}}{c} \tag{3.14}$$

$$\eta_{TEM} = -\frac{E_z^+}{H_\phi^+} = j\eta \frac{H_0^{(2)}(\beta\rho)}{H_1^{(2)}(\beta\rho)} \tag{3.15}$$

The fact that the derivation only considers the outwardly propagating radial waves allows us study the matching at the post-to-waveguide transition. A very interesting aspect of the fields in equations 3.11 through 3.15 is that they are exactly the same as an infinite-line current source. This equivalence is due to the lack of z-directed dependance in an infinite-line source directed

along $\hat{\mathbf{z}}$. In the propagation constant, this implies $\beta_\rho = \beta$, which is exactly the same as the TEM case for a radial waveguide. Moreover, for $\beta\rho \rightarrow large$, $\eta_{TEM} \rightarrow \eta_0$.

3.5 Infinite-Line Current Source Model Comparison with Radial Waveguide

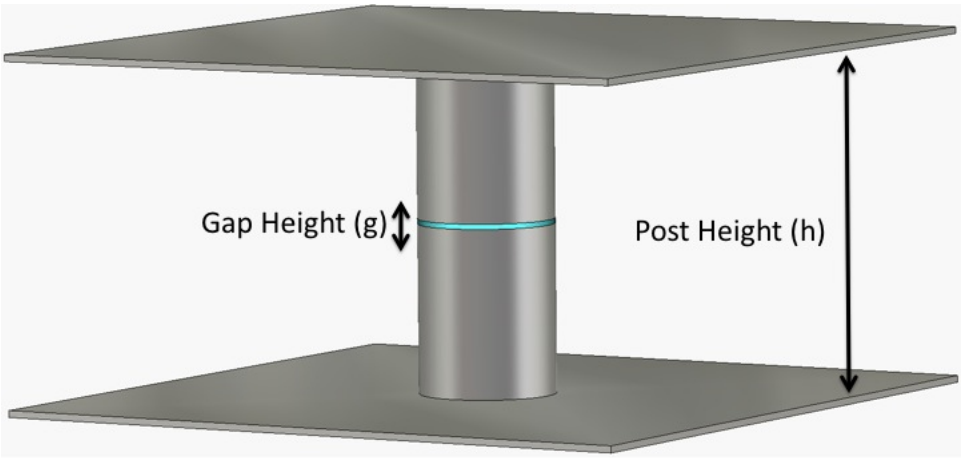

Figure 3.23: Cylindrical post loaded with parallel plates

To further investigate the the infinite-line current model and the radial waveguide, the first analysis of Fig. 3.23 involves a PEC post loaded with two parallel plates and an ENZ gap launcher. Perfectly matched layer (PML) boundary conditions were used to compare only the radiated fields to the ones derived in equations 3.11 through 3.15. By using a PML boundary condition, a layer is placed around the structure that perfectly absorbs all of the radiating fields at the boundary. So in a sense, it is not a boundary condition but a perfectly absorbing layer, which causes all the fields to become evanescent

beyond the boundary, and any small reflection will be acutely attenuated on the return path. Figure 3.24 demonstrates the nature of the cylindrical waves for the waveguide in Fig. 3.23 with a PML around the structure.

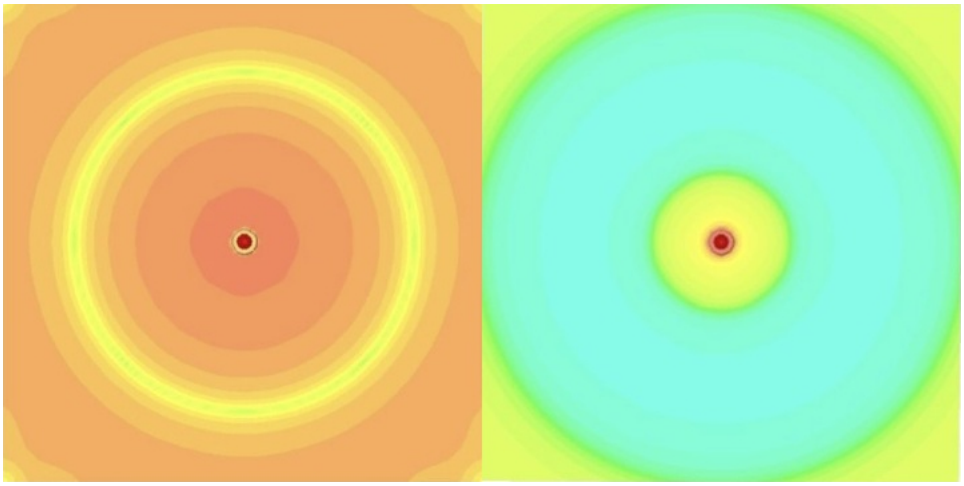

Figure 3.24: H_ϕ and E_z of TEM cylindrical wave

A comparison was done between the analytical models developed in equations 3.11–3.15 and the full-wave simulation of Fig. 3.23 with a Drude Model ENZ gap, f_p = 0.63 GHz, (g) of 2 mm, post height (h) = 50 mm. Figure 3.25 shows the wave impedance comparison between equation 3.15 and $\eta = -\frac{E_z}{H_\phi}$ at a radial distance ρ from the radiating post. We can see that the models match very well. However, there is a small ripple in the full-wave simulation.

Figure 3.26 was generated by varying the lengths of the loading plates on the post. Two interesting points are that the matching frequency and matching input resistance change very little with the length of the loading

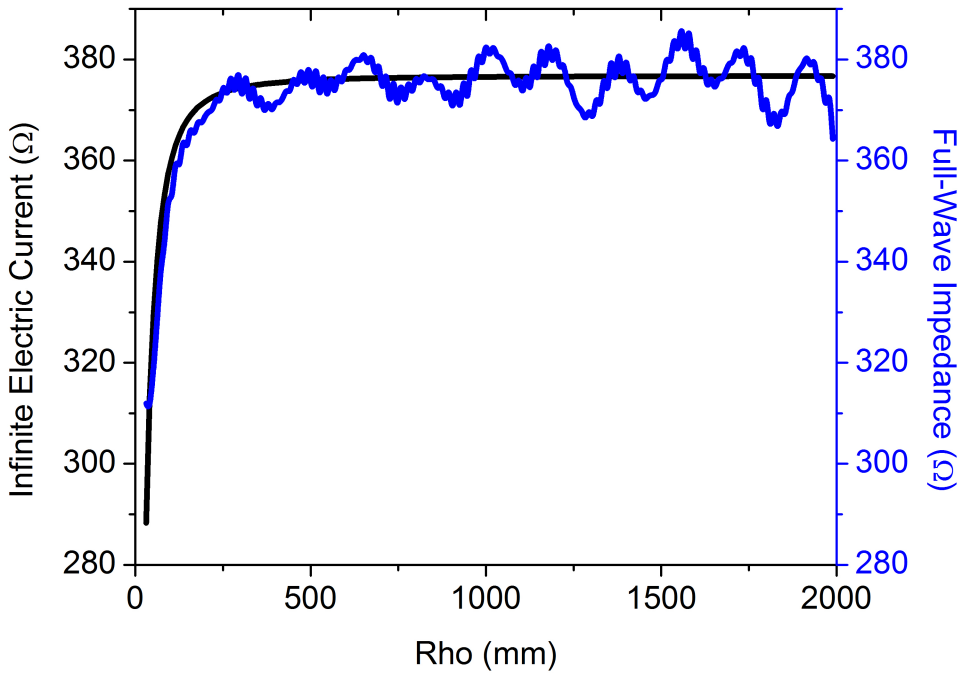

Figure 3.25: Analytical models compared against full-wave simulation of Fig. 3.23 with Drude model ENZ, $f_p = 0.63$ GHz, g = 2 mm, h = 50 mm.

plates. Another being, the matching input resistance is approximately half of the wave impedance of a particular plate length. This could be a general result for matching this waveguide structure, which is quite interesting.

3.6 Radial Waveguide Post Matching Characterization

To gain better intuition of the input impedance about the radial waveguide in Fig. 3.23 with an air gap launcher, Fig. 3.27 was used to compare the full wave simulation with two different simple LC models. In Fig. 3.27,

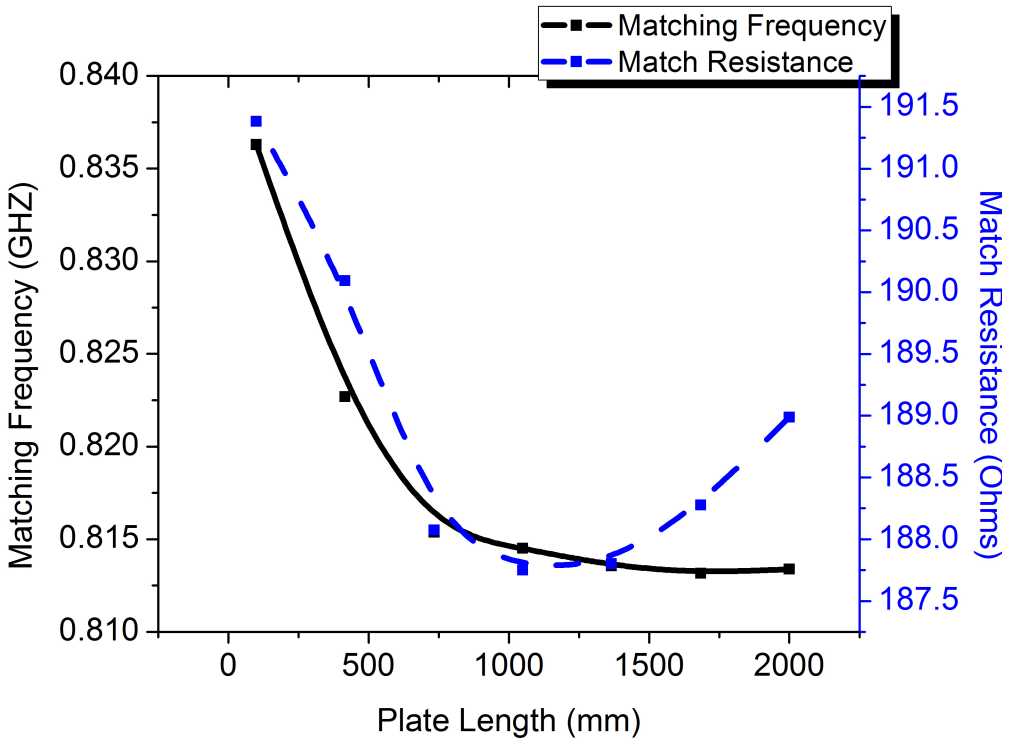

Figure 3.26: Study of plate length on antenna parameters with Drude model ENZ, $f_p = 0.63$ GHz, g = 2 mm, h = 50 mm.

the CST curve represents the resonant frequency of different gap heights from 0.5 mm to 2 mm by post-porcessing the E_z and H_ϕ fields from CST. In the same figure, LC is a simple static model, and Hankel is a based on equations 3.11–3.15. While the curves' behavior matches well, the static LC model was normalized by 52 and the Hankel-based model was normalized by 12. The discrepancy in the static LC model is that it assumes constant fields. Both the Hankel and static models do not include outer capacitances and inductances or discontinuities in the waveguide. Therefore, the differences are do to the

complicated nature of the equivalent circuit model of the waveguide; however, it is very clear that the overall behavior is very much an LC circuit. Moreover, the general sensitivity of the antenna parameters such as matching frequency and bandwidth will be dominated by the post gap height and radius. Therefore, we can see the tuning do to the gap height, since its separation distance strongly effects the effective input capacitance of the waveguide. By increasing the separation distance, we can tune the resonant frequency up or down.

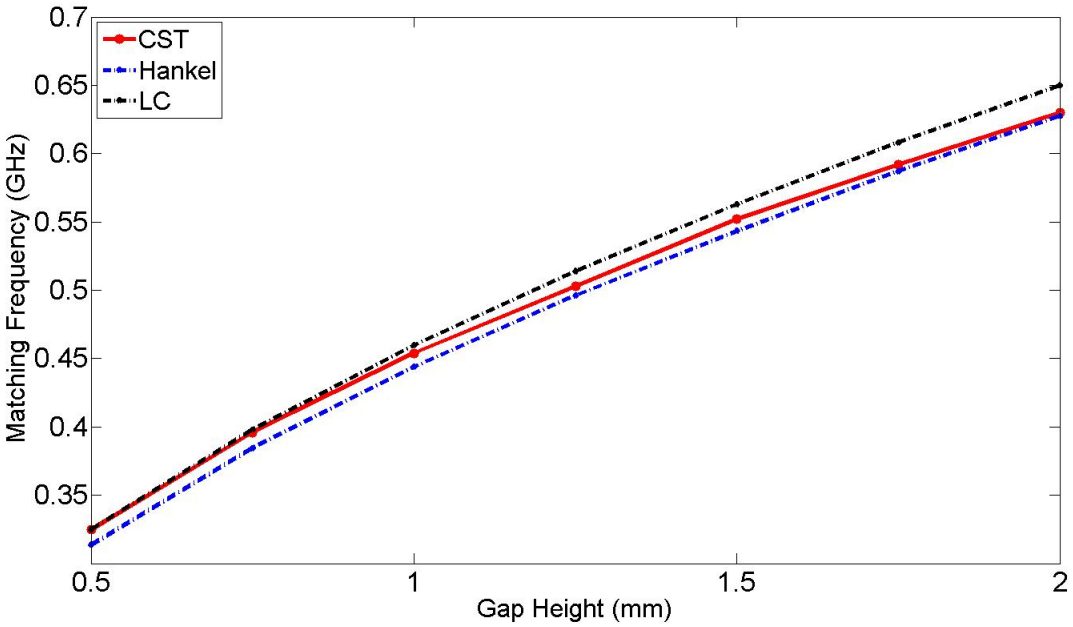

Figure 3.27: LC equivalent circuit model of parallel-plate radial waveguide, h = 50 mm, $\epsilon_r = 1$.

3.6.1 Gap height investigation

Figures 3.28 and 3.29 verify the key antenna parameter sensitivity to the feed gap height for the radial waveguide. By using PML boundary conditions

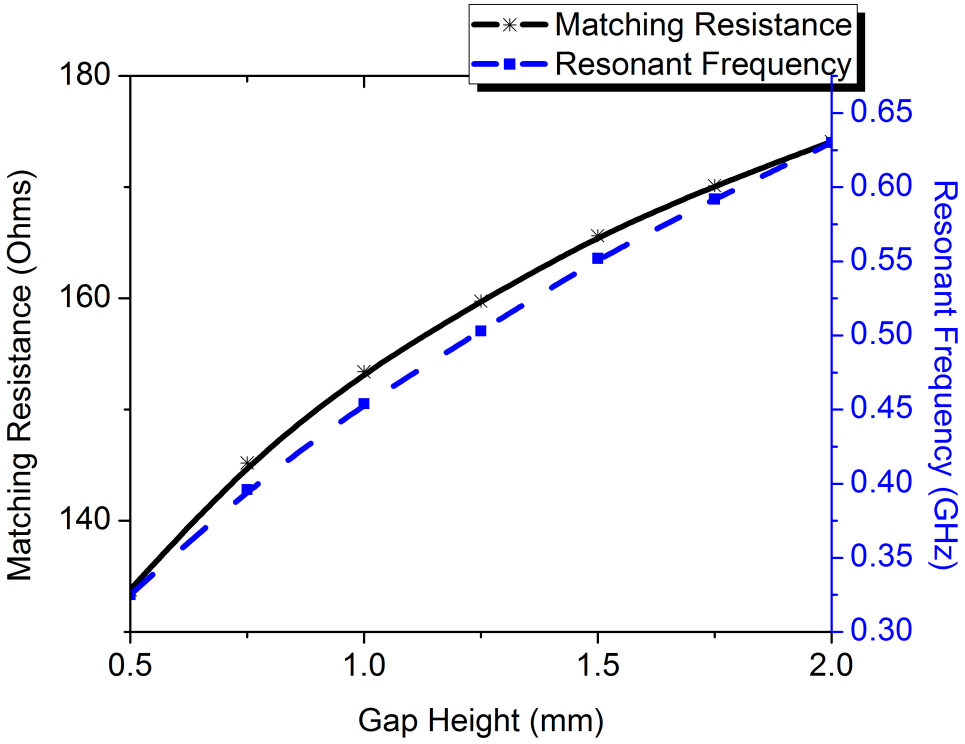

Figure 3.28: Matching frequency and matching input resistance over gap height, h = 50 mm, $\epsilon_r = 1$.

in the full-wave simulations, we are able to isolate the post to parallel-plate waveguide interface. From these figures, we can see that the curves follow a typical LC equivalent circuit model, where the matching frequency follows $\frac{1}{2\pi\sqrt{L_{eq}C_{eq}}}$. While the values of L_{eq} and C_{eq} are somewhat complicated by field discontinuities and non-constant field intensities, the trends in figures 3.28 and 3.29 clearly validate the LC equivalent circuit behavior. One interesting point is that the fractional bandwidth increases fairly strongly, $\approx 8.5\%$ per mm, for an increasing gap height, as shown in figure 3.29, which is due to the increase

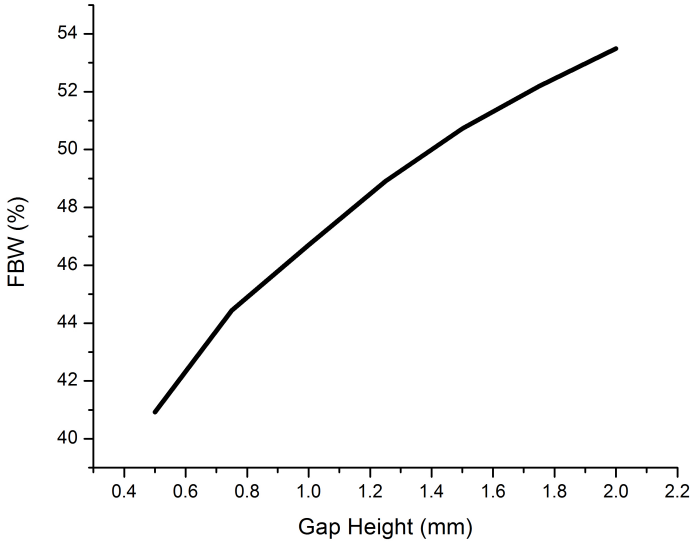

Figure 3.29: Fractional bandwidth over gap height, h = 50 mm, $\epsilon_r = 1$.

in the resonant frequency of the waveguide.

Figures 3.28 and 3.29 were calculated by using the full-wave simulator CST and varying the post feed height. The feed input resistance was found by finding its value at the frequency that corresponded to a zero input reactance, shown in Fig. 3.30. Then, the scattering parameters were normalized to the input resistance at the zero reactance frequency, which corresponded to a *matched* antenna feed. The return loss for the matched ENZ gap parallel-plate radial waveguide is given in Fig. 3.31. From figures 3.30 and 3.31, we can see it is possible and practical to match the radial waveguide with a coaxial cable to the radial waveguide.

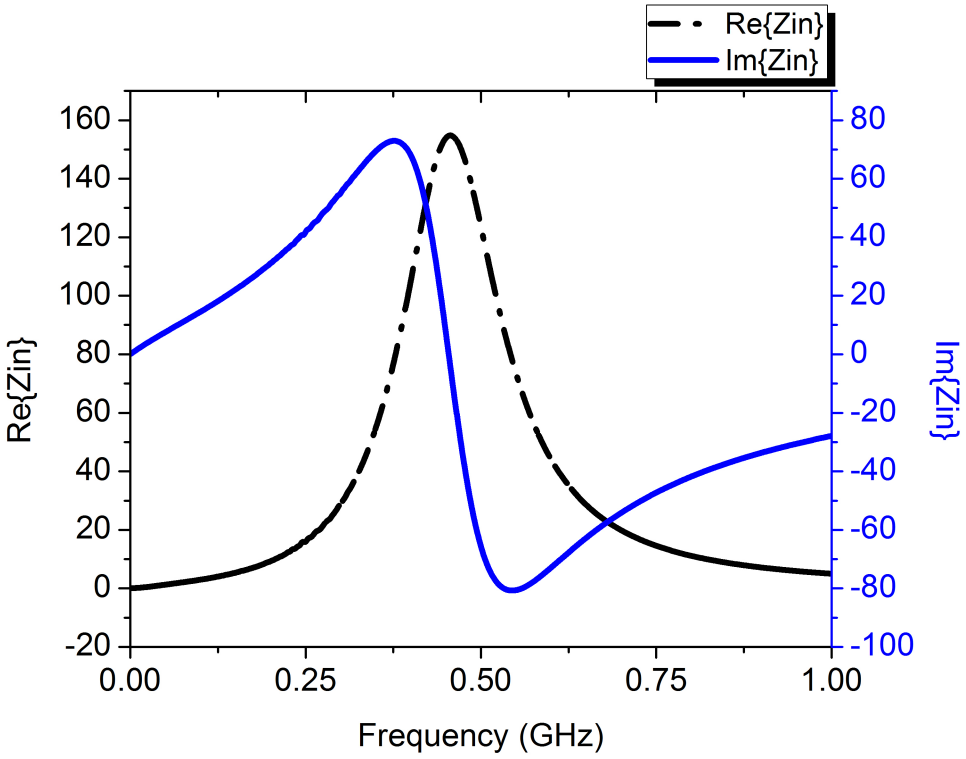

Figure 3.30: Input impedance for ENZ gap, g = 0.5 mm, h = 50 mm, f_p = 0.325 GHz.

3.6.2 Comparisons between DPS and ENZ gap launchers

The matching input resistance and matching frequencies for the air-gap and ENZ gap are plotted in figures 3.32 and 3.33. For the air gap, we can see that for h = 50 mm and g = 0.25 mm, the antenna is approaching the resonance of a $\frac{\lambda}{2}$ dipole with f_0 = 0.3 GHz. As the gap height is increased, the effective input capacitance is decreased and tuned to a higher resonant frequency. The plasma frequency of the ENZ structure is an additional tuning mechanism, along with the gap height, for the waveguide or antenna. This

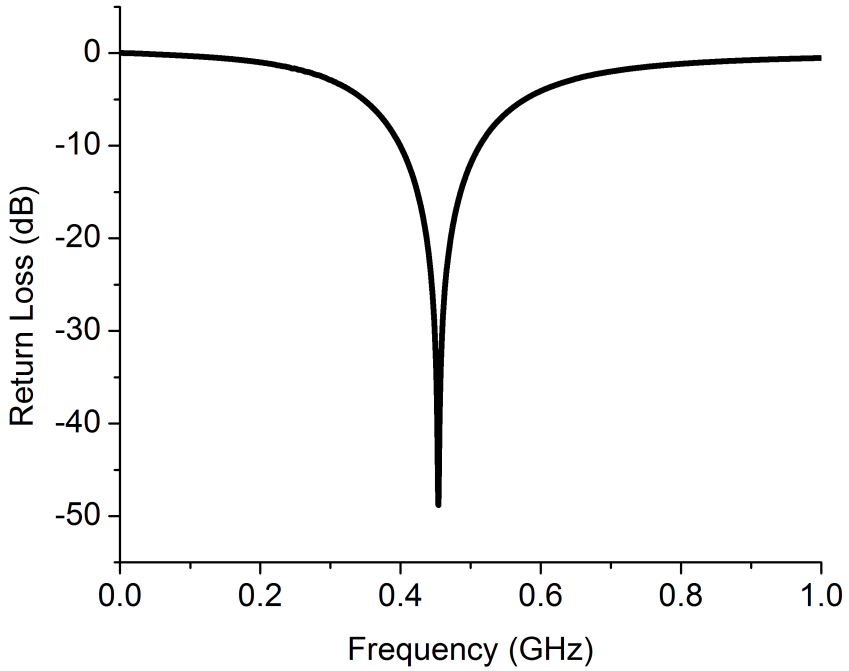

Figure 3.31: Matched ENZ gap post, g = 0.5 mm, h = 50 mm, f_p = 0.325 GHz.

can be shown in Fig. 3.34. Here we see that for a given gap height of 2 mm, the antenna can be further tuned by the use of the ENZ material.

The curves in figures 3.32 and 3.33 are almost identical except that the ENZ gap generally resonates at a higher frequency than the air gap. While the impedances between the two look much different, one can notice that at the higher air gap frequencies, the corresponding input resistances are higher, which almost exactly correspond to the ENZ gap input resistances at those frequencies. Therefore, the matching input resistance does not depend on

whether one uses an air or an ENZ gap launcher.

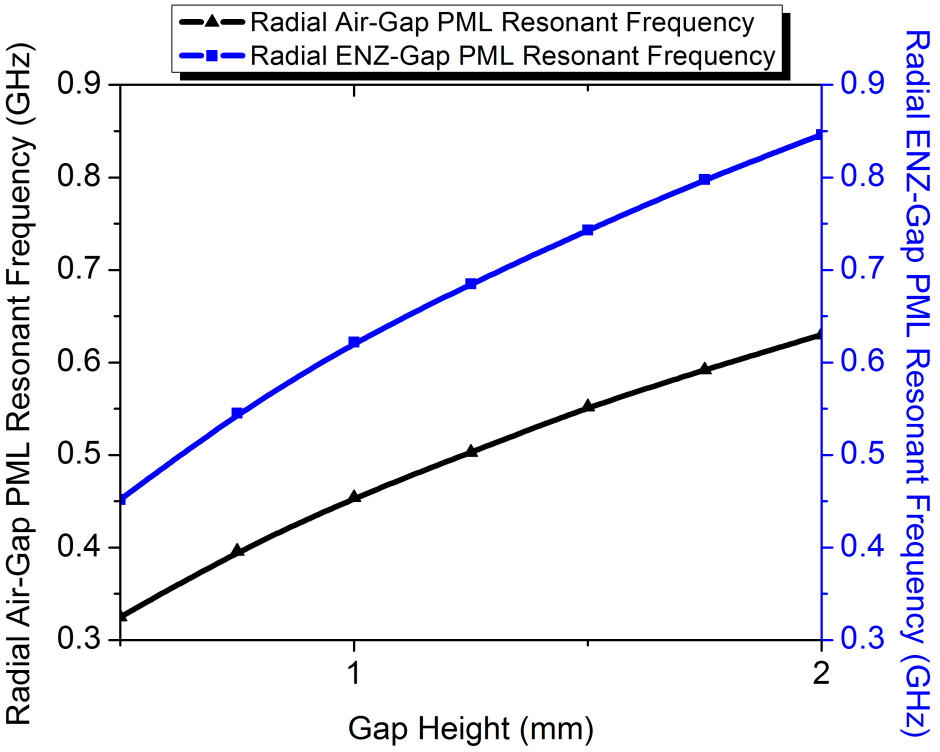

Figure 3.32: Resonant frequency over gap height, h = 50 mm for PML.

3.7 Scattering at the Free-Space/Waveguide Boundary

When a free-space boundary condition is used to simulate an antenna structure, the bandwidth is severely minimized and the operating frequency is moved to a significantly different frequency. This can be explained by the mismatch at the parallel-plate/free-space boundary. This mismatch causes a strong reflection; therefore, a standing-wave is produced in the structure. This standing-wave behavior causes the structure to operate more as a resonator

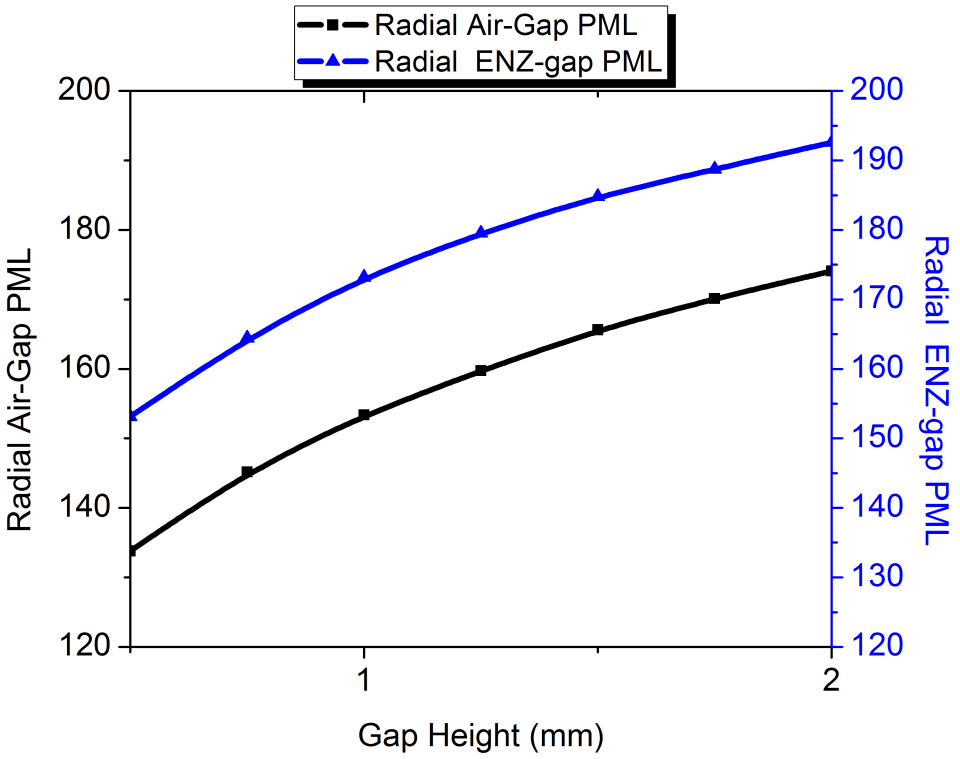

Figure 3.33: Input resistance over gap height, h = 50 mm.

than a radiator because more of the energy is stored in the near-field of the antenna, which is evident by the increased Q (reduced bandwidth) of the antenna. Under this reasoning, by tapering the parallel-plates, we can match the antenna to the surrounding free-space environment, thereby, increasing the efficiency and bandwidth of the antenna.

Figure 3.35 shows the resonant frequencies of an air gap radial waveguide with and without tapering. We see in Fig. 3.35 that the tapering allows a much tighter variation in the resonant frequencies over the non-tapered case. The lower variation in resonate frequencies will lead to a better FBW over

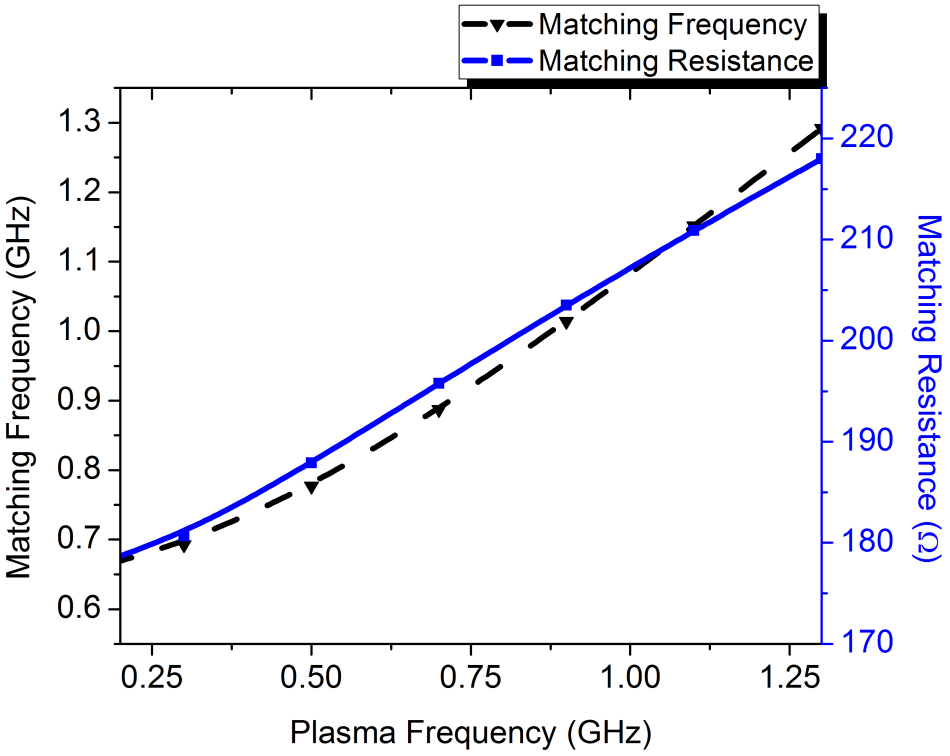

Figure 3.34: Input resistance and matching frequency for g = 2 mm, h = 50 mm for various plasma frequencies.

the non-tapered case. Figure 3.36 shows the difference for air-gap and ENZ-gap tapered radial waveguides in free space. As can be seen in the figure, the variation in matching resistance is tighter for the ENZ-gap ($\Delta R_{in} = 70\Omega$) than is for the air-gap ($\Delta R_{in} = 120\Omega$). Therefore, the FBW should be better in the ENZ, tapered, free space case. Also, the ENZ matching input resistance is higher than the air gap, since the ENZ typically resonates at a higher frequency than does the air gap in this frequency band.

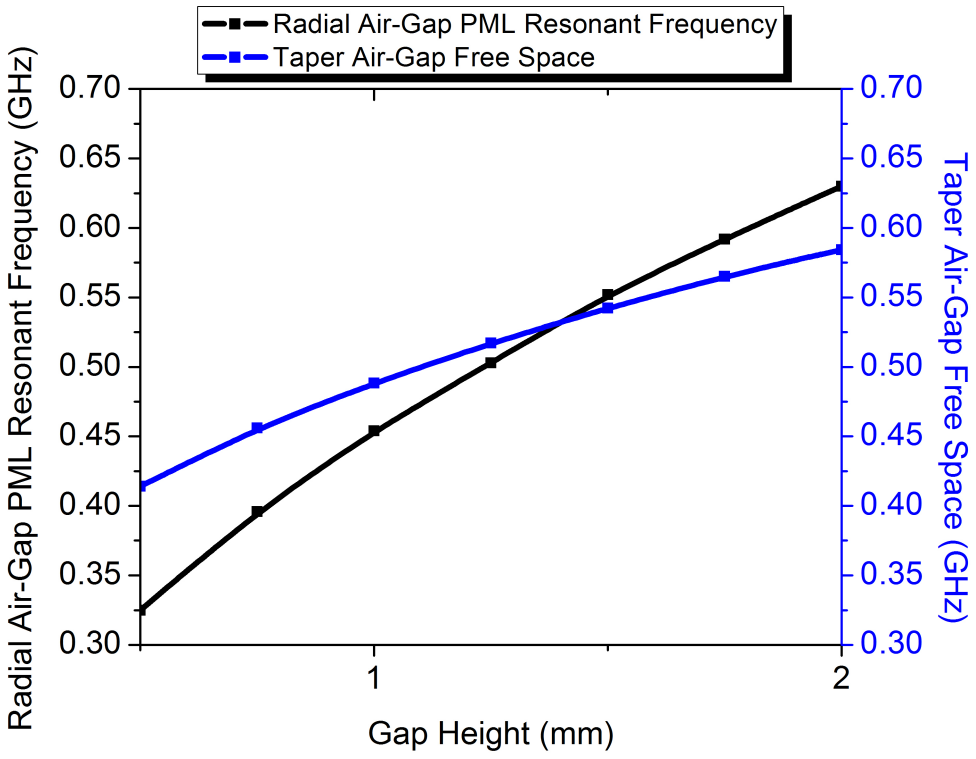

Figure 3.35: Resonant frequency versus gap height for tapered and DPS gap launchers for PML and free space boundaries, h = 50 mm.

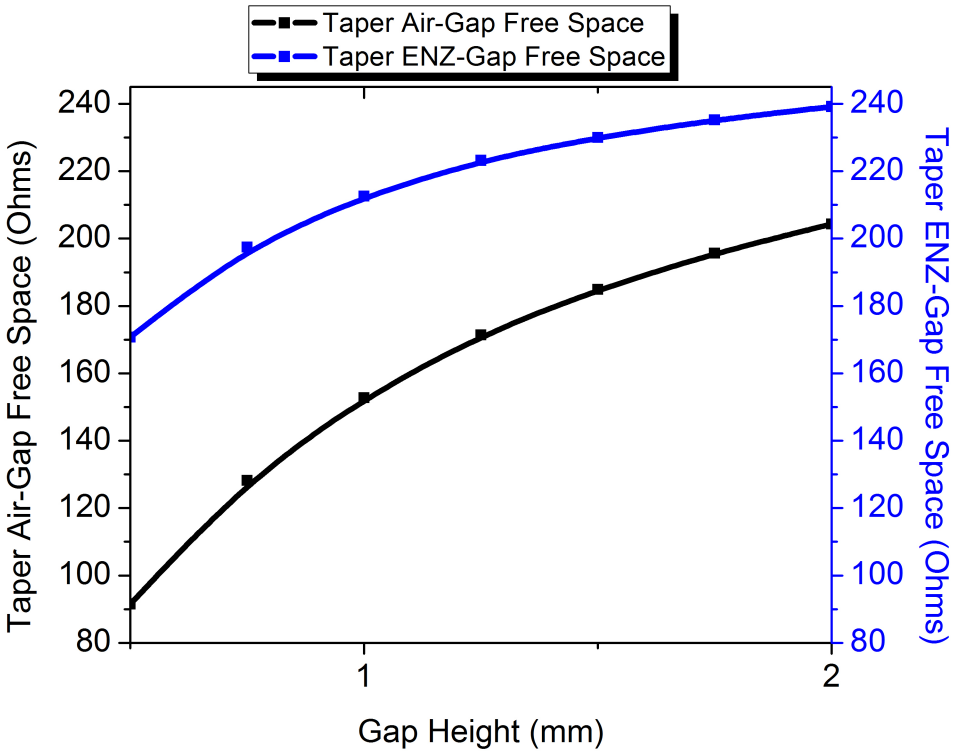

Figure 3.36: Matching input resistance versus gap height for tapered DPS and ENZ gap launchers, h = 50 mm.

Chapter 4

Conclusion

Multifarious engineering applications using the ENZ concept exist: filter design, coaxial-to-waveguide matching, frequency mixing, phase tailoring of electromagnetic sources, and increased directivity. In this work several applications where derived and shown using the ENZ concept. This type of metamaterial has many interesting properties, which reveal new and exciting physical phenomena. Our group has applied this concept to several ideas to optimize existing RF and microwave devices, yet we still uncover new applications regularly. One of the most compelling aspects of our work is the fabrication and experimental verification of this innovative anomalous electromagnetic behavior.

This work has shown that the concept of epsilon-near-zero supertunneling agrees very well in theory, simulation, and measured experimental results. We showed that we could analytically write expressions for the reflection coefficient of junctions between two, or more, rectangular waveguides with disparate geometries. Additionally, we showed that at the cutoff of the inner-connecting rectangular waveguide, the ENZ channel impedance "sees" a proportional wave impedance of the outer waveguides due to the compensation between a low ef-

fective permittivity and a ultra-narrow rectangular waveguide entrance. This agreement between analytical models, simulation, and experiment is exciting and shows a new method for designing waveguiding components and antenna structures.

In Chapter 1, a brief introduction to the concept of metamaterials was shown. Additionally, work was reviewed and re-simulated by in the works of A. Alú and M. Silveirinha. M. Silveirinha provided excellent work in developing exact analytical models describing the supercoupling phenomenon between two waveguides connected via an arbitrary $\epsilon = 0$ channel. A. Alú further developed the work to show the transmission line model describing an ENZ channel rather than an $\epsilon = 0$ channel, and that reciprocity could be used for ENZ matching for waveguides and antennas. Alú also gave models describing the lumped-element value of the evanescent reactances at the ENZ entrances. Additionally, Alú clearly showed that the ENZ resonant phenomena is different than the classic Fabry-Perot resonance commonly found in resonators.

In Chapter 2, experimental work was done which verified the supercoupling concept for another independent experimental setup. The experiment was done using rectangular waveguides connected by another rectangular waveguide at cutoff. The simulation and experimental results were very similar.

In Chapter 3, coax-to-waveguide matching was demonstrated by using the $\frac{\lambda}{2}$ electric field variation across the ENZ channel to match to a standard 50 Ω cable. A multi-band pyramidal ENZ horn antenna was also simulated that

showed excellent radiation and matching performance. Work was also done in fully characterizing a radial waveguide with air and ENZ-gaps.

Bibliography

[1] Engheta, N. and Ziolkowski, R.W., *Metamaterials: Physics and Engineering Exploration*, *Wiley-IEEE Press*, 2006.

[2] Caloz, C. and Itoh, T., *Electromagnetic Metamaterials: Transmission Line Theory and Microwave Applications: The Engineering Approach*, *Wiley-IEEE Press*, 2006.

[3] Rotman, W., "Plasma Simulation by Artificial Dielectrics and Parallel-plate Media", *Antennas and Propagation, IRE Transactions on*, vol. 10, no. 1, pp. 82–95, 1962.

[4] Pendry, J.B., "Negative Refraction Makes a Perfect Lens", *Physical Review Letters*, vol. 85, no. 18, pp. 3966–3969, 2000.

[5] Smith, D.R. and Padilla, W.J. and Vier, DC and Nemat-Nasser, S.C. and Schultz, S., "Composite Medium with Simultaneously Negative Permeability and Permittivity", *Physical Review Letters*, vol. 84, no. 18, pp. 4184–4187, 2000.

[6] Caloz, C. and Itoh, T., "Invited-Novel Microwave Devices and Structures Based on the Transmission Line Approach of Meta-Materials", *IEEE MTT-S International Microwave Symposium Digest*, pp. 195–198, 2003.

[7] Alù, A. and Silveirinha, M.G. and Salandrino, A. and Engheta, N., "Epsilon-Near-Zero Metamaterials and Electromagnetic Sources: Tailoring the Radiation Phase Pattern", *Physical Review B*, vol. 75, no. 15, pp. 155410, 2007.

[8] Alù, A. and Engheta, N., "Cloaking a Sensor", *Physical Review Letters*, vol. 102, no. 23, pp. 233901 2009.

[9] Alù, A. and Engheta, N., "Pairing an Epsilon-Negative Slab With a Mu-Negative Slab: Resonance, Tunneling and Transparency", *IEEE Transactions on Antennas and Propagation*, vol. 52, no. 5, pp. 2558–2571, 2003.

[10] Caloz, C. and Itoh, T., "Transmission Line Approach of Left-Handed (LH) Materials and Microstrip Implementation of an Artificial LH Transmission Line", *IEEE Transactions on Antennas and Propagation*, vol. 51, no. 10, pp. 1159–1166, 2004.

[11] Veselago, V.G., "The Electrodynamics of Substances with Simultaneously Negative Values of ϵ and μ", *Physics-Uspekhi*, vol. 10, no. 4, pp. 509–514, 1968.

[12] Alù, A. and Silveirinha, M.G. and Engheta, N., "Transmission-line Analysis of ϵ -near-zero–filled Narrow Channels", *Physical Review E*, vol. 78, no. 1, pp. 016604, July, 2008.

[13] Silveirinha, M. G. and Engheta, N., "Tunneling of Electromagnetic Energy through Subwavelength Channels and Bends using ϵ-Near-Zero Ma-

terials", *Physical Review Letters*, vol. 97, no. 15, pp. 157403, Oct., 2006.

[14] Silveirinha, M. G. and Engheta, N., "Theory of supercoupling, squeezing wave energy, and field confinement in narrow channels and tight bends using ϵ near-zero metamaterials", *Phys. Rev. B*, vol. 76, no. 24, pp. 245109, Dec., 2007.

[15] Alù, A. and Engheta, N., "Coaxial-to-Waveguide Matching With ε-Near-Zero Ultranarrow Channels and Bends", *IEEE Transactions on Antennas and Propagation*, vol. 58, no. 2, pp. 328–339, 2010.

[16] Edwards, B. and Alù, A. and Young, M.E. and Silveirinha, M. G. and Engheta, N., "Experimental Verification of Epsilon-Near-Zero Metamaterial Coupling and Energy Squeezing Using a Microwave Waveguide", *Physical Review Letters*, vol. 100, no. 3, pp. 044905 -044905-4, Jan., 2008.

[17] Edwards, B. and Alù, A. and Silveirinha, M. G. and Engheta, N., "Reflectionless Sharp Bends and Corners in Waveguides Using Epsilon-Near-Zero Effects", *Journal of Applied Physics*, vol. 105, no. 4, pp. 044905 -044905-4, Feb., 2009.

[18] Liu, Ruopeng and Cheng, Qiang and Hand, Thomas and Mock, Jack J. and Cui, Tie Jun and Cummer, Steven A. and Smith, David R., "Experimental Demonstration of Electromagnetic Tunneling Through an Epsilon-Near-Zero Metamaterial at Microwave Frequencies", *Phys. Rev. Lett.*, vol. 100, no. 2, pp. 023903, Jan., 2008.

[19] Balanis, C.A., *Advanced Engineering Electromagnetics*, John Wiley & Sons, New York, New York, 1989.

[20] Montgomery, C.G. and Dicke, R.H. and Purcell, E.M., *Principles of Microwave Circuits*, Dover Publications Inc., New York, New York, 1965.

[21] Ramo, S. and Whinnery, T.R. and van Duzer, T., *Fields and Waves in Communication Electronics*, John Wiley & Sons, New York, New York, 1965.

Vita

Jason C. Soric was born in Houston, Texas November 11, 1976. He received his B.S.E.E. in May 2006 from The University of Texas at Austin. While working on his undergraduate degree, he worked as a science tutor at Austin Community College, and was a researcher in the Electrical Engineering Research Laboratory (EERL) and the Wireless Networking and Communications Group (WNCG) in Austin. Additionally, he interned at Ball Aerospace and Technologies Corporation in Westminster, Colorado. Upon graduation, Jason worked as a Manufacturing Engineer at Harris Microwave Communications Division in San Antonio, Texas.

In 2008, Jason started his graduate studies at The University of Texas at Austin with emphasis on Electromagnetics and RF/Microwave Circuit Design. In 2009, he interned at Raytheon Space and Airborne Systems in El Segundo, California. Currently, he is working with Dr. John H. Davis and Dr. Andrea Alú's Metamaterials and Plasmonics Research Group in Austin, Texas.

Email address: soric.jason@gmail.com

This thesis was typeset with LaTeX[†] by the author.

[†]LaTeX is a document preparation system developed by Leslie Lamport as a special version of Donald Knuth's TeX Program.